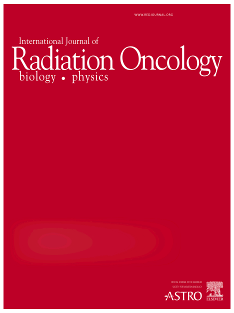

Micro-imaging of brain cancer radiotherapy using phase-contrast computed tomography

G.E. Barbone, A. Bravin, P. Romanelli, A. Mittone, D. Bucci, T. Gaaβ, G. Le Duc, S. Auweter, M. Reiser, M.J. Kraiger, M. Hrabě de Angelis, G. Battaglia, P. Coan

PII: S0360-3016(18)30614-X

DOI: 10.1016/j.ijrobp.2018.03.063

Reference: ROB 24908

To appear in: *International Journal of Radiation Oncology • Biology • Physics*

Received Date: 10 March 2017

Revised Date: 23 March 2018

Accepted Date: 29 March 2018

Please cite this article as: Barbone GE, Bravin A, Romanelli P, Mittone A, Bucci D, Gaaβ T, Le Duc G, Auweter S, Reiser M, Kraiger MJ, Hrabě de Angelis M, Battaglia G, Coan P, Micro-imaging of brain cancer radiotherapy using phase-contrast computed tomography, *International Journal of Radiation Oncology • Biology • Physics* (2018), doi: 10.1016/j.ijrobp.2018.03.063.

Micro-imaging of brain cancer radiotherapy using phase-contrast computed tomography

G. E. Barbone[1], A. Bravin[2], P. Romanelli[3], A. Mittone[2], D. Bucci[4], T. Gaaβ[5], G. Le Duc[2], S. Auweter[5], M. Reiser[5], M. J. Kraiger[6], M. Hrabě de Angelis[6,7,8], G. Battaglia[4], P. Coan[1,5]

1. Department of Physics, Ludwig Maximilians University, 1 Am Coulombwall, Garching, 85748, Germany. 2. European Synchrotron Radiation Facility (ESRF), Grenoble 38043, France. 3. Brain Radiosurgery, Cyberknife Center, CDI, Via Saint Bon 20, 20147, Milano, Italy 4. Department of Molecular Pathology, Neuropharmacology Section, I.R.C.C.S. Neuromed, 86077 Pozzilli (IS), Italy. 5. Department of Clinical Radiology, Ludwig Maximilians University, 15 D Marchioninistr., Munich, 81377 Germany, 6. Institute of Experimental Genetics and the German Mouse Clinic, Helmholtz Zentrum München, German Research Center for Environmental Health, Ingolstädter Landstrasse 1, Neuherberg, 85764 Germany, 7. Chair of Experimental Genetics, School of Life Science Weihenstephan, Technische Universität München, Alte Akademie 8, 85354 Freising, Germany. 8. German Center for Diabetes Research (DZD), Ingolstädter Landstr. 1, 85764 Neuherberg, Germany.

Mr. Barbone has nothing to disclose.
Dr. Bravin has nothing to disclose.
Dr. Romanelli has nothing to disclose.
Dr. Mittone has nothing to disclose.
Dr. Gaaβ has nothing to disclose.
Dr. Bucci has nothing to disclose.
Dr. Le Duc has nothing to disclose.
Dr. Auweter has nothing to disclose.
Dr. Reiser reports personal fees from Ludwig-Maximilians-University Munich, Germany, grants from DFG Cluster of Excellence Munich-Centre for Advanced Photonics (MAP), the DFG Gottfried Wilhelm Leibniz program and the European Research Council (ERC, FP7, StG 240142), grants from EUROBIOIMAGING, grants from German National Cohort, grants from Munich Cluster of Excellence - M4 - Imaging, grants from BMBF German Center for Lung Diseases , grants from BMBF German Center for Cardiovascular Diseases, outside the submitted work.
Dr. Krainger has nothing to disclose.
Dr. Hrabě de Angelis has nothing to disclose.
Dr. Battaglia has nothing to disclose.
Dr. Coan has nothing to disclose.

Acknowledgments:

Authors would like to acknowledge the financial support from the Deutsche Forschungsgemeinschaft (cluster of excellence) - Munich Center for Advanced Photonics (EXE158) and of the European SYRA3 COST Action TD1205 for networking and financing scientific missions within this project. Authors also thank the ESRF for provision of beamtime and laboratory facilities, Dr H. Requardt for the technical support, Dr. E. Brun for the help in the initial phase of this work, as well as the electronic, computing, and software assistance of the ESRF. Finally, authors thank Prof. B. Ertl-Wagner from the LMU Klinikum Grosshadern for supporting this collaboration, the German Mouse Clinic of the Helmholtz Zentrum München for allowing us to use their 9.4T MRI scanner, and the German Federal Ministry of Education and Research (Infrafrontier grant 01KX1012) (MHdA).

Micro-imaging of brain cancer radiotherapy using phase-contrast computed tomography

Abstract:

Purpose: Experimental neuroimaging provides a wide range of methods for the visualization of brain anatomical morphology down to sub-cellular detail. Still, each technique-specific detection mechanism presents compromises between achievable field-of-view size, spatial resolution or nervous-tissue sensitivity, leading e.g. to partial sample coverage, unresolved morphological structure or sparse labeling of neuronal populations, and often also to obligatory sample dissections or other sample-invasive manipulations. X-ray Phase Contrast CT (PCI-CT) is an experimental imaging methodology, which simultaneously provides micrometric spatial resolution, high soft-tissue sensitivity and *ex-vivo* full-organ rodent brain coverage without any need for sample dissection, staining/labeling or contrast agent injection. In this work, we explore the benefits and limitations of PCI-CT use for the *in-vitro* imaging of normal and cancerous brain neuro-morphology after *in-vivo* treatment with synchrotron-generated X-ray Microbeam Radiation Therapy (MRT), a spatially fractionated experimental high-dose radiosurgery. The goals are the visualization of MRT treatment effects on nervous tissue, and qualitative comparison of results to histology and high-field MRI.

Methods: MRT was administered *in-vivo* to the brain of both healthy and cancer-bearing rats. Forty-five days post-treatment, brain organs were dissected out and imaged *ex-vivo* via propagation-based PCI-CT.

Results: PCI-CT visualizes brain anatomy and micro-vasculature in 3D, and distinguishes cancerous tissue morphology, necrosis, and intra-tumor accumulation of iron and calcium deposits. Moreover, PCI-CT detects the effects of MRT throughout treatment target areas, e.g. the formation of micrometer-thick radiation-induced tissue ablations. Observed neuro-structures were confirmed by histology and immunohistochemistry, and related to micro-MRI data.

Conclusions: PCI-CT enables a unique 3D neuroimaging approach for *ex-vivo* studies on small animal models, in that it concurrently delivers high-resolution insight on local brain tissue morphology in both normal and cancerous micro-milieu, localizes radiosurgical damage, and highlights deep micro-vasculature. This method could assist experimental small-animal neurology studies in the *post-mortem* evaluation of neuropathology or treatment effects.

Introduction:

Spatial fractionation of radiation dose delivery, by relying on the so-called tissue-sparing dose-volume effect, is an emerging issue in neuro-radiosurgery and might represent a new avenue for effective and less invasive brain cancer radiotherapy[1]. X-ray Microbeam Radiation Therapy (MRT)[2] features the reshaping of a laminar synchrotron beam into arrays of highly collimated quasi-parallel micrometer-thick microbeams. This technique administers spatially-restricted peak doses of many hundreds of Grays indiscriminately to healthy and tumor tissues alike, and was proven to selectively disrupt tumor tissues, while being well tolerated by healthy ones[3]. Its success in tumor treatment has been attributed to differences in tissue radio-resistance[4] and a diminished reorganization and repair capability of tumor vessel networks with respect to healthy ones[5,6]. The reported efficacy of MRT, though, remains a complex and partly-unanswered question, and neuroimaging methodologies able to perform rigorous follow-ups of this pre-clinical technique's effects would be of paramount importance to gain a better understanding of MRT's tissue-dependent dose response.

Modern neuroimaging is a fast-growing field, today able to provide high-quality anatomical and functional maps of the Central Nervous System (CNS) from full organs down to sub-cellular structure. MRI and CT can both attain 3D micrometric resolution via small-animal micro-MRI and micro-CT scanners. Recent *in-vivo* advances include ultra-high-field small animal brain imaging[7]. Brain tumor angiogenesis can also be studied via micro-MR angiography, at spatial resolutions of 60 µm and after contrast agent administration[8]. Conventional X-ray micro-CT, for its part, is able to assess the presence of tumors in small animals *in-vivo*[9] after contrast media injection, but otherwise affords soft-tissue sensitivity that is, in absence of contrast agents, rather low.

Ex-vivo high-resolution MRI after active staining[10] allows the study of full-organ brain tissue microstructure down to 10-25µm isotropic resolution, quantitative regional volumetric measurements, and the elaboration of several distinct image contrasts, so-called *proton stains*, highlighting specific anatomical features. When applied *ex-vivo*, these imaging methods are referred to as MR-histologies, even though they do not fully discriminate single cells. MRI-based morphologic phenotyping of neuroanatomy has been instrumental in non-destructively creating 3D full-organ atlases of a number of animal models[11,12], and is used for the full-organ study of neuro-pathologies and of neuro-development[13]. Moreover, by imaging local molecular water diffusion to detect microstructural differences in bio-tissues, MRI permits the calculation of 3D axonal inter-voxel connectivity via diffusion tensor imaging (DTI) and fiber tractography[14], giving access to a unique full-organ view of (white-matter) brain organization[15,16]. Interestingly, cutting-edge micro-MRIs, combining different kinds of MR contrasts, are able to resolve the laminar anatomy and underlying cyto-architecture of the hippocampus (e.g. using DTI and 60 microns in-plane resolution)[17], are sensitive to brain tumor cell density[18], detect tumor invasion[19], recover complex 3D maps of vascular micro-architecture and can measure vascular angiogenesis[20]. Functional small-animal positron emission tomography (PET), for its part, provides dynamic images of the bio-distributions of radioactive tracers and allows a wide range of full-organ and *in-vivo* longitudinal follow-up studies for neuro-pharmacological testing and neurodegenerative disease characterization[21]. PET, though, is a relatively low-resolution imaging tool, and offers indirect-only morphological imaging.

Histology and immunohistochemistry, gold standard methodologies in neuroscience, instead, offer both sub-cellular resolution and tailored stain-dependent tissue contrasts. Still, they remain highly sample-invasive techniques (the specimen being sectioned by a microtome to produce planar histological slices), are often time consuming and mostly still lack the capability to directly render complex neuron and vessel networks developing in 3D space. The gap between histology and MRI/CT-based approaches has been filled by other powerful ultra-high resolution neuroimaging research methodologies, having varying degree of sample-invasiveness, resolution and fields of view: two-photon microscopy, for example, detects deep-brain calcium dynamics by using fluorescent indicators, reveals large-scale neuronal activity *in-vivo*, and renders a functional and structural image of single neurons within localized neural populations[22,23] at the cellular and subcellular level. This method can also be combined with electrical recordings of neuronal activity[24] to obtain precious morphological and functional information simultaneously. *Ex-vivo* local 3D properties of single glial, astrocytic and neuronal cyto-architecture, as well as subcellular detail and synaptic organization, can also be rendered today by combining 3D light microscopic methodology with deep and uniform antibody labeling procedures[25] even after long-term sample storage. On the other hand, novel optical tissue-clearing (TC) methods enable full-organ 3D fluorescence imaging[26,27] and the *ex-vivo* study of cellular and vascular organization throughout entire organisms[28]. Finally, optical coherence tomography (OCT), which is an ultra-fast technique applied *in-vivo*, permits minimally-invasive local endoscopic optical biopsies[29], revealing both brain[30] and tumor morphology[31]. Furthermore, swept-source optical coherence Doppler tomography (SS-ODT), sensitive to dynamic and transient chances in 3D cerebral blood-flow, enables *in-vivo* functional micro-circulatory imaging of deep brain vasculature at depths down to 3.2mm[32].

Overall, the great diversification of novel neuroimaging technology gives neuroscientists a much-expanded tool-kit with which to tackle the complexity of the CNS. Still, all these methods have evident limitations, which are more or less critical depending on the desired application: some struggle to achieve sample-coverage of more than a few millimeters (OCT, SS-ODT) or present spatial restrictions of the neuronal area of visualization (e.g. cellular visualizations are limited to the staining-area covered by calcium indicator dyes or by the antibody-label penetration depth). Others afford an only partial labelling of cell populations (fluorescence-based methodologies), or have very sample-invasive procedures (TC and deep antibody labeling, for example), which hamper any prospects of future *in-vivo* application. Full-organ rodent brain coverage, a non-specific both nervous- and tumor-tissue-sensitive contrast mechanism, and micrometric resolution are instead concurrent requirements to reliably study local effects in the brain of fractionated high-dose radiosurgery on both normal and cancerous neuro-morphology.

X-ray Phase Contrast CT (PCI-CT) is an experimental high-resolution imaging technique of interest to biomedical research for its ability to visualize soft-matter biological tissues[33–36], providing a sensitivity 2 to 3 order of magnitudes higher than that of absorption CT[37,38] in the hard X-ray regime. We presume that PCI-CT might be able to contribute to the study of X-ray irradiation effects on brain tissue, since the technique was reported to provide high nervous-tissue contrast complementary to MRI[39]. Various PCI techniques have already been applied to neuroimaging: grating interferometry enables high-resolution depictions of tumor tissues, the hippocampus and cerebellum regions[40], white and gray matter[41], the *substantia nigra* structure[42] and brain myelin sheaths[43]. More localized brain tissue studies, using crystal interferometry, single-shot propagation-based phase-contrast imaging or other PCI-CT techniques, have identified blood micro-vessels[44], the molecular layer and the granular layer in the cerebellum, and have shown how multimodal brain imaging can lead to deeper insight compared to single-technique studies[39]. Finally, PCI techniques were able to effectively localize cancer masses within the brain[40], to demarcate tumor vs. heathy tissue boundaries[45], to visualize cancerous tissue morphology[46,47] and to identify cancer-driven tissue degeneration[48,49] without addition of contrast-agent.

All of these results together show that PCI-CT is a unique *ex-vivo* high-resolution neuroimaging technique, providing high degrees of morphological precision, full-organ rodent brain coverage and sensitivity in the 3D visualization of both healthy and pathological CNS tissues. Moreover, PCI-CT overcomes some of the burdens and limitations of histological work-up, by allowing a dissection-free 3D virtual direct measurement of deep morphology within large samples (several cm in both width and height). Thus, PCI-CT-based high-resolution structural neuroimaging could provide new insight to ongoing oncology research on small-animals involving micrometric dose-fractionation in radiotherapy. Here we investigate the possibility of visualizing the biological marks of an X-ray microbeam irradiation protocol, by evaluating rat brain PCI-CT images and comparing them to histology and MRI, with the goal of validating PCI-CT as a viable imaging technique for *post-mortem* MRT-treatment evaluation.

Methods:

Animal preparation:

Six eight-week-old male Fisher[50] rats were implanted with the 9L glioblastoma (GBM) cell line[51] in the right hemisphere, following published protocols[52,53]. Three rats, used as controls, were not implanted with tumors. Fifteen days after tumor cell inoculation, all animals (9 in total) were treated with different MRT protocols (see MRT irradiation protocols in the following section of the Methods), and then sacrificed 1.5 months post-treatment. After animal sacrifice, all 9 brain samples were dissected out, fixed in 10% formalin solution (no negative influence in PCI experiments[54]) and stored in plastic tubes until imaging analysis. All operative procedures related to animal care strictly conformed to guidelines of the French Government and were approved by the ethical committee of the European Synchrotron (ESRF).

MRT irradiation:

Both radiotherapy and imaging were performed at the Biomedical Beamline ID17 of the ESRF. The first beamline hutch, stationed 42 m away from a wiggler-based synchrotron X-ray source and devoted to MRT treatment, receives filtered X-rays of wide spectral range (median energy: 90 keV; spectral range: 50-350 keV) and of high dose rates[55] (>14 kGy/s). Via a specifically engineered tungsten multi-slit collimator[56], the beam is spatially fractionated into a comb-like dose profile, producing 25-75 µm-thick high-dose microbeams (peak doses > 100 Gy) interspersed by much wider valleys, where lower well-tolerated doses are delivered to biological samples[57]. Animals were anesthetized (4% isoflurane inhalation, for induction, and ketamine, 100 mg/kg, + xylazine, 10 mg/kg, i.p., for maintenance) and positioned on a stereotactic frame[53]. Rat brains were then irradiated with microbeams 50 µm in width and 1 cm in height, both uni-directionally and by 90 degree cross-firing[58]. Inter-microbeam spacing was varied between different sample irradiations, determining center-to-center (c-t-c) inter-microbeam distances of 200 or 400 µm. Moreover, three microbeam peak entrance doses were selected (250, 400 and 600 Gy, measured at 2 mm depth). A total 1 cm^2 square-shaped irradiation area was delivered posteriorly and laterally to the cranium bregma point. MRT valley doses for 50 µm thick microbeams with 200 µm c-t-c distance are reported[59] to scale the peak dose by a factor of ~ 1/27, leading to estimated valley doses of around 9, 15 and 22 Gy (for the MRT treatments with peak doses respectively at 250, 400 and 600 Gy). In the 400 µm c-t-c distance case, the scaling factor is reported[60] to be ~ 1/57, leading, as expected, to lower valley doses, respectively of 4, 7 and 11 Gy. Since dose scales linearly, 2-direction cross-firing irradiations lead to a doubling of the dose in the valleys.

Sample-specific irradiation parameters:

sample 1: tumor-bearing, treated with unidirectional 600 Gy 400 µm c-t-c MRT, valley dose ~ 11 Gy;

sample 2: tumor-bearing, treated with unidirectional 400 Gy 400 μm c-t-c MRT, valley dose ~ 7 Gy;

sample 3: tumor-bearing, treated with unidirectional 600 Gy 200 μm c-t-c MRT, valley dose ~ 22 Gy;

sample 4: tumor-bearing, treated with unidirectional 400 Gy 200 μm c-t-c MRT, valley dose ~ 15 Gy;

sample 5: tumor-bearing, treated with cross-firing 400*2 Gy 400 μm c-t-c MRT, valley dose ~ 14 Gy;

sample 6: tumor-bearing, treated with cross-firing 250*2 Gy 400 μm c-t-c MRT, valley dose ~ 8 Gy;

sample 7: healthy, treated with cross-firing 400*2 Gy 400 μm c-t-c MRT, valley dose ~ 14 Gy;

sample 8: healthy, treated with cross-firing 250*2 Gy 400 μm c-t-c MRT, valley dose ~ 8 Gy;

sample 9: healthy and untreated.

Propagation-based Phase Contrast Imaging:

Post-mortem imaging was performed in the ID17 imaging hutch (150 m away from the source), using a standard propagation-based PCI (PBI) experimental setup[61–63]. The 9 extracted brain samples were placed in a formalin-filled Falcon tube and illuminated with highly-collimated quasi-coherent monochromatic 26 keV X-rays. A low-noise 2k CCD FReLoN camera[64] was selected as imaging detector, in turn coupled to an 8 μm lens-based optics (sample-to-detector distance: 7 m; detector field-of-view (FoV): 16 mm; voxel size: 8x8x8 μm^3). We acquired PCI-CT image-datasets with 3000 projections over 360 degrees in half acquisition[34] (total acquisition time: ~2.5 h per sample), achieving an overall horizontal FoV of 30 mm. Vertically, motorized sample translation of sub-pixel precision enables subsequent CT scans at different heights, and an overall vertical FoV of up to 100 mm. The combined FoV of 30x100 mm^2 is suitable for full-organ rodent brain imaging. PCI-CT images were reconstructed using standard filtered back-projection algorithms for CT, and a phase retrieval algorithm[45,65] specific for single distance PBI was used to extract the sample phase-contrast map. Arising CT ring artefacts were in large part removed from reconstructed CT slices using a published correction tool[66].

Vessel network renderings:

Brain vessel-network segmentations were obtained using a region growing algorithm (applied to sample 9 datasets), and the 3D renderings were produced using the commercial software VG Studio MAX[67]. Moreover, brain vessel 2D maximum intensity projection maps were computed over 200 consecutive slices (from sample 2 and 4 data) by awarding to each particular pixel location its maximum value over all images in the stack (i.e. the maximum intensity z-projection function in ImageJ software (NIH, USA), a method which highlights bright 3D features and maps them onto a 2D plane).

Histology & Immunohistochemistry:

Hematoxylin/eosin (H&E) histology was performed on samples 2-9. Nissl staining, Perls' Prussian Blue staining, specific for iron deposits, and Alizarin Red S staining, specific for calcium deposits, were performed after imaging on two MRT-irradiated and tumor-bearing brain samples (sample 2 and 6). Formalin-fixed brains were included in paraffin and 15 µm sections were cut on a microtome. The Perls' Prussian Blue consists of potassium ferrocyanide, which reacts with ferritin to yield a blue-colored compound. For Alizarin Red S staining, sections were hydrated in descending series of ethanol and immersed in 2% Alizarin red S (2% in distilled water pH 4.3) for 45 sec. For immunohistochemistry deparaffinised sections from sample 6 were soaked in 3% hydrogen peroxide, to block endogenous peroxidase activity, and incubated overnight with polyclonal goat anti-ionized calcium binding adaptor molecule-1 (Iba-1) (1:1000, ab-107159, Abcam, Cambridge, United Kingdom), monoclonal mouse anti-glial fibrillary acidic protein (GFAP) (1:100, G-3893, Sigma-Aldrich, St. Louis, MO), with polyclonal rabbit anti-Ki-67 (1:20, RM-9106, Thermo Fisher Scientific, Fremont, CA), and with rabbit anti-laminin (1:100, NB300-144, Novus Biological, Littleton, CO), and then for 1h with secondary biotinylated anti-goat, anti-mouse and anti-rabbit antibodies, respectively (1:200; Vector Laboratories, Burlingame, CA). Sections were treated with 10 mM, pH 6.0, citrate buffer, and heated in a microwave for 30 min for antigen retrieval. Control staining was performed without the primary antibodies. The immunoreaction was performed with 3,3-diaminobenzidine tetrachloride (ABC Elite kit; Vector Laboratories).

MRI Experiment:

One MRT-irradiated tumor-bearing brain sample (sample 1) was additionally *ex-vivo* imaged inside a formalin-filled Falcon tube with a pre-clinical 9.4 T MRI scanner (BioSpec 94/20 USR, Bruker). Since all PCI neuro-images in this work were taken *post-mortem*, the specimen was also MRI-imaged *ex-vivo* in exactly the same sample conditions and environment as for PCI-CT, in order to obtain a comparable MRI dataset. Axial brain images were taken using the manufacture's two channel array RX/TX cryo probe (Z125365). Coronal brain images were acquired using an eight channel RX array volume coil (T20030V3) optimized for rat brain imaging in combination with a quadrature TX volume resonator (T12054V3). We acquired both T1- and T2-weighted sequences optimized for brain anatomical high-resolution imaging.

Axial MRI sequences specifications:

2D**-T2 MSME**: Bruker Biospin 2D-T2map-MSME sequence; echo images: 8; echo spacing: 8.63 ms; TR: 4000 ms; N-averages: 8; FOV: 20*15 mm²; slice thickness: 0.8 mm; pixel size: 63*59 µm²; acquisition matrix size: 320*256; bandwidth: 78125 Hz; duration: 2 h 16 m 32 s.

3D-**T1 FLASH:** Bruker Biospin T1_FLASH_3D_SWI sequence; flip angle: 25°; TE: 4.74 ms; TR: 100 ms; N-averages: 6; FOV: 25*15*5 mm³; pixel size: 48.8*46.9*78 µm³; acquisition matrix size: 512*320*64; Anti-alias in slice direction: 1.313; bandwidth: 100000 Hz; duration: 4 h 28 m 48 s.

Coronal MRI sequences specifications:

2D**-DTI:** Bruker Biospin DTI_EPI sequence; diffusion directions: 30; A0 reference images: 5; max. b-value: 1634.03 s/mm²; TE: 19.96 ms; TR: 3000 ms; N-averages: 35; FOV: 15*15 mm²; pixel size: 138.9*156.3 µm²; slice thickness: 0.8 mm; acquisition matrix size: 108*60; reconstruction matrix size: 108*96; Partial FT: 1.6; bandwidth: 340909.1 Hz; duration: 1 h 1 m 15 s.

3D**-T1 RARE:** Bruker Biospin T1_RARE sequence; TE: 8.35 ms; RareFactor: 2; TR: 1000 ms; inversion delay: 400 ms; N-averages: 8; FOV: 15x15x16 mm³; pixel size:

53.6*53.6*250 µm³; acquisition matrix size: 256*256*64; bandwidth: 50000 Hz; duration: 9 h 57 m 20 s.

3D-**T2* MGE**: Bruker Biospin T2_star_MGE sequence; flip angle: 30°; TE: 3.46 ms; TR: 150 ms; N-averages: 10; FOV: 15*15*4 mm³; pixel size: 58.6*58.6*250 µm³; acquisition matrix size: 256*192*16; reconstruction matrix size: 256*256*16; Partial FT: 1.33; bandwidth: 69444.4 Hz; duration: 1 h 16 m 48 s.

Results:

Imaging brain anatomy

High resolution X-ray PCI images (Fig. 1) of an excised control rat brain sample (sample 9) showcase the achievable sensitivity to brain anatomical detail of this imaging method, which measures small differences in local tissue density and refractivity. Sagittal (Fig. 1a) and coronal (Fig. 1b-d) slices exhibit full-organ brain structural images, including cerebellar, cortical, thalamic and hypo-thalamic areas. Brain sub-region anatomy is visualized in the coronal slices, e.g. the striatum region and lateral ventricles filled with choroid plexi (1b), the hippocampus and the cell layers within Ammon's Horn and the Dentate Gyrus (1c), cerebellar granular and molecular layers of gray matter and the white matter of the arbor vitae (1d). Phase-contrast signal (1e) in the granular cell layer (*stratum granulosum*) of the hippocampal Dentate Gyrus is compared (1f) and superimposed (1g) to H&E histological staining. A formalin-filled third ventricle is also visible in the PCI image, corresponding in the histological slice to an area empty of tissues. Zoom-ins of the striated architecture of the caudate-putamen, of the ventricles, of the layers of the hippocampal formation and of the cerebellar arbor vitae can be found in **Suppl. Figure 7**.

Figure 1| X-ray phase-contrast CT of rat brain anatomy.

(a) sagittal slice displaying somatosensory and visual areas of the cortex (CTX), the thalamus (TH), hypothalamus (HY) and midbrain (MB), the lobules of the cerebellum (CB) with distinct molecular (mo) and granular (gr) layers, and large portions of the medulla (MY) and pons (P) regions. **(b)** coronal section of cortical (CTX), thalamic (TH) and hypothalamic (HY) regions, with view of the third ventricle (V3) and lateral ventricles (LV) filled with choroid plexi (cp), and of the striated architecture of the caudate-putamen of the dorsal striatum (dSRT) perfused by long bright blood-vessels (BV). **(c)** coronal view of the dorsal hippocampus, divided in the layers within Hammon's Horn (CA) and in the Dentate Gyrus (DG). **(d)**

cerebellar (CB) slice, showing the arbor vitae (arb) and lobules (lob) and contrast in both the granular (gr) and molecular (mo) layers of gray matter, part of the forth ventricle system (V4) and a large section of the medulla region (MY). PCI **(e)**, H&E histology **(f)** and superposition of the two techniques **(g)** illustrate the structure of the granular cell layer (*stratum granulosum,* sg) of the hippocampal Dentate Gyrus. The third ventricle (V3) is filled with low-signal formalin in PCI **(e)** and is empty in the histology slice **(g)**.

Imaging glioblastoma tumor

Fig. 2 shows how the PCI contrast mechanism enables the detection of GBM tumor tissue morphology. Cancerous tissue from implanted 9L glioblastoma cells (marked as GBM in Fig. 2, data from samples 1-5) was observed via PCI within brain striatum, thalamic (2a, 2e) and hypothalamic regions (Fig. 2c-d), as well as partly growing inside lateral ventricles (Fig. 2a). GBM neoplasms can be recognized as regions of higher phase-contrast relatively to surrounding normal brain parenchyma and to contralateral non-implanted brain hemispheres (Fig. 2a, 2c-f). Core GBM lesions feature hyper-cellularity, comprised of a mix of densely-packed astrocytes, blood vessels and other cells, an abnormal hyper-dense cellular microenvironment, which modifies local refractive properties and densities compared to those within normal nervous tissue, thereby influences PCI signal and seems to lead to local hyper-intensity within GBMs (Fig. 2a, 2c-f).

Figures 2a-b highlight PCI intensity differences within one selected tumor-bearing brain sample: some of the lowest gray-levels pertain to the low-density formalin environment surrounding the sample and within formalin-filled ventricles and blood vessels (samples were formalin-fixed and vasculature was at least partially perfused). Normal nervous tissue presents average gray-levels slightly above those pertaining to formalin (see cortex and amygdalar gray-levels in Fig. 2a-b). Peaks in the gray-value profile seem instead to correspond to local vasculature, which was not completely washed during perfusion: vessels partially filled with densely-packed blood cells or with collapsed endothelial membranes, create local hyper-density areas detected by the PCI technique. PCI signal within GBM tissue was found on average higher than nervous tissue in all inoculated cerebra, with signal contributions coming from all sources of hyper-density: notably the typical densely-packed cancerous cellularity and the increased and aberrant vascularization (Fig. 2 c-e), and even localized tumor-driven blood extravasations or tissue calcification (Fig. 2e), all contribute to give rise respectively to the highest average gray-levels and to intra-GBM signal peaks. Other areas of low PCI signal arise from necrotic areas at the center of tumor masses, affording troughs within GBM gray-value profiles (Fig. 2a-c, 2e): cell death causes decreased cellularity and even the formation of empty cystic cavities, which diminishes the local density and local refraction effects and affords a PCI signal similar (or even lower) to that of formalin-filled brain ventricles (see trough within the GMB gray-level profile in Fig. 2b, marked as necrotic in origin). PCI signal is admittedly non-specific in nature, in that different features can give rise to similar PCI intensity levels. Fig. 2a-b show that it is indeed difficult to differentiate formalin from an empty vessel from a cyst in a necrotic area (all hypo-intense features) based on PCI signal alone, as is difficult differentiating between filled vessels and tumor tissue (both hyper-intense features). In these cases, gray-level-based structure differentiation must be complemented by morphological observations. What is though possible with PCI, is to differentiate between low-intensity and high-intensity features, and, most importantly, to recognize these structures within normal nervous tissue.

The high phase-contrast between areas of tumor-driven parenchymal cell destruction and surrounding normal tissues enables the visualization of tumor micro-morphology: broad anatomical deformation and compression, caused by neoplasm growth, are visualized in all tumor-bearing samples (e.g. deformed lateral ventricle above the tumor mass in Fig. 2f-g). In Fig. 2c and 2d, we observe the invasion by infiltrating malignant tissue of areas neighboring core lesions (tentacle-like tissue morphology and high PCI-signal areas at the periphery of and beyond the main tumor mass). Thorough identification of GBM tissue composition (and of microglial infiltrating cells) by immunohistochemical analysis can be found in Fig. 5. Figures 2e and 2e' show a typical pathologic feature of GBM, i.e. tumor cells forming pseudopalisades[68], characterized by interconnected hyper-dense layers of tumor-cell accumulation surrounding a central clear zone of hypoxia-driven necrosis. Tissue apoptosis and necrosis are, in fact, caused by the malfunction of the vessel at the center of the pseudopalisade after tumor-growth-driven endothelial injury, vaso-occlusion and intravascular thrombosis (a central bright vessel is visible within all pseudopalisades in 2e). The pseudopalisades successively also secrete angiogenic factors leading to microvascular proliferation and hyperplasia in adjacent regions[68] (hyperplasia is visible in Fig. 2e). All the morphologic features of pseudopalisades observed via PCI in 2e were confirmed by the H&E histology in 2e'.

A comparison of phase-contrast vs. histological tumor tissue characterization can be observed in Fig. 2f vs. 2g: cortical and hypothalamic tissue, a formalin-filled ventricle and blood-filled vasculature, and, most importantly, GBM tissue are visualized via both techniques. A PCI zoom-in on GBM morphology (Fig. 2h) highlights, by comparison (2j) and superposition (2i) to the corresponding histological slice, how PCI signal differences are closely related to the cellularity differences between normal and cancerous tissues present in the histology. Further immunohistochemical characterization of PCI signal within tumor tissue and within blood vessels is carried out respectively in Fig. 5 and in Fig. 3.

Figure 2| X-ray phase-contrast CT of tumor anatomy.

(a) a GBM-bearing PCI slice and its corresponding 16bit gray-value profile **(b)**, measured along the pink line in **(a)**, illustrates PCI contrast between different brain anatomical features: surrounding formalin and a formalin-filled ventricle (f and ffV, red), formalin-filled blood vessels (ffBV, orange), cortical and amygdalar normal tissue (CTX and AMG, blue), blood-filled blood vessels (bfBV, turquoise), glioblastoma tumor tissue (GBM, green) and necrotic tissue (nec, black). Colored arrows point to features in **(a)** and to corresponding gray-value levels in **(b)**. **(c)** GBM tissue appears as an asymmetric bright area within the thalamus and hypothalamus. The tumor is necrotizing at the core (nec, dark-pixels area) and infiltrating surrounding tissues (inf). **(d)** GBM tissue infiltration (inf), with islets of tumor cells and tentacular cancer regions invading normal tissue. **(e)** a large necrotizing (nec) GBM growing near a deformed hippocampus (HIP) and lateral ventricle (LV). PCI shows sign of potential tissue calcification and tumor-driven iron-rich blood extravasation (cal/fe) leading to the agglomeration of hyper-dense intra-tumoral clusters (very bright areas in PCI). PCI also shows pseudopalisading (pP) tumor cell hyper-dense accumulation surrounding a hypo-dense hypoxia-driven necrotic region and an occluded central vessel (ocV). Nearby microvascular hyperplasia (mVH) is caused by proangiogenic factor secretion by the hypoxic pseudopalisades. **(e')** H&E histology confirms the morphology of GBM pseudopalisades seen in **(e)**. **(f-g)** comparison between PCI **(f)** and H&E histology **(g)** of cortex (CTX), lateral ventricle (LV), hypothalamus (HY) and GBM morphology. Zoom-in of PCI **(h)**, histology **(l)** and superposition of the two **(i)** illustrate the local structure of GBM tissue invading surrounding hypothalamic (HY) tissue. Blood-filled blood vessels (bfBV) are annotated throughout the figure.

Imaging brain vasculature

Brain blood vessels, which irrigate the encephalon both superficially and internally, can be recognized throughout PCI data of normal and tumor-bearing tissues as both low-density (hypo-intense) and high-density (hyper-intense) interconnected tubular structures of size down to a few tens of µm (Fig. 3a). The hyper-dense features can be segmented, to provide 3D vessel-network trees, or superimposed by addition of several consecutive image-slices, to provide 2D maximum intensity projection maps (2D MIP, see Methods section), with the tree-shaped volumetric morphology of these tubular features (Fig. 3f-k) suggesting their vascular nature. Immunohistochemistry of laminin, a marker for blood vessels, confirmed their presence, and helped characterize the meaning of the PCI gray-levels: hyper-dense structures consisting of collapsed or blood-filled blood vessels correspond to bright tubules in PCI (Fig. 3b-d vs. 3b'-d'), and hypo-dense empty vessels correspond to dark formalin-filled tubules in PCI (Fig. 3e vs. 3e'). H&E staining confirmed the presence of collapsed blood vessels (Fig. 3b''), of vessels half-filled with blood red cells (3c''), of collapsed vessel with packed red blood cells (3d''), and of empty blood vessel (3e''). The full laminin histology vs. the corresponding PCI image can be found in **Suppl. Fig. 8**.

Larger superficial blood vessels with thick hyper-dense endothelial membranes, residing in the subarachnoid space, are visualized as bright tubes covering most of the external organ (Fig. 3i). Intra-cortical vasculature and capillaries, branching radially inwards from the outer layers toward the inner brain (Fig. 3a, 3f-g), are visible as bright tubules, when collapsed or when filled or half-filled with red blood cells, or as dark tubules, when non-collapsed and formalin-filled. The full-organ angio-architecture, comprised of anterior (ACA), middle (MCA) and posterior cerebral arteries (PCA) can be followed on 2D MIPs both in healthy samples (Fig. 3f-h), where it is notably hierarchically organized and evenly distributed, and in tumor-bearing samples (Fig. 3i-k), which, as is well-known[69], features densely-packed immature, tortuous and disorganized tumor vasculature in and around the malignant lesions (data from sample 2, 4 and 9). Deep hyper-dense micro-vascularization was detected extending to the center of the organ as an organized and tidy network in a healthy brain (Fig. 3h), or as a chaotic bundle wrapping around the

GBM in a tumor-bearing cerebrum (Fig. 3j). Undeniably, it is difficult to differentiate between signals from local aberrant vessel anatomy and GBM tissue hyper-cellularity within the core of neoplasms in 2D, as both anatomical components are present at the same time: a close-reading of local 3D morphology and of relative gray-level differences is needed in this case (Fig. 3i-k). Vasculature within healthy parenchyma, as the tumor-free vasculature imaging in Fig. 3f-h demonstrates, is instead much easier to recognize. Further 2D and 3D PCI-based renderings of tumor and vascular anatomy can be found in **Suppl. Fig. 9**.

Figure 3| X-ray PCI-CT, immunohistochemistry and H&E staining of blood vessel anatomy.
(a) Coronal PCI slice at the -5.4 mm from bregma level of a rat brain bearing a GBM shows both low-density (black arrows) and high-density (red arrows) tubular interconnected structures. **(b,c,d,e)** details of PCI vascular imaging taken from the squares 1, 2, 3 and 4 highlighted in **(a)**. **(b',c',d',e')** details from the immunohistochemistry of laminin, a marker of blood vessels performed at the same bregma level as the PCI in **(a)** and taken from the same 1 to 4 squares (a full laminin histology slice can be found in **Suppl. Fig. 8**). Note the presence of collapsed or blood-filled blood vessels (**b', c', d'**), corresponding to bright high-density tubular structures (red arrows) in (**a**), and empty blood vessels (**e'**), corresponding to dark low-density formalin-filled tubular structures (black arrows) in (**a**). H&E staining at the same bregma level as the PCI in **(a)** showing a collapsed capillary **(b'')**, a half-empty vessel with few red blood cells **(c'')**, a vessel filled with packed red blood cells and an empty blood vessel (**e''**). Red arrows indicate vessels corresponding to bright PCI signal and black arrows indicate vessels corresponding to dark PCI signal. Axial **(f, i)** and coronal **(g,k)** 2D maximum intensity projection maps (MIP, see Methods on vessel network renderings) highlight blood-filled, collapsed and thick-walled vascular anatomy: large superficial (supBV) and microscopic (> 16 µm-thick) intra-cortical blood vessels (intBV) appear as intense tubular structures (red arrows point towards them), i.e. anterior (ACA), middle (MCA) and posterior cerebral arteries (PCA) and related micro-vasculature, in both healthy **(f,g)** and tumor-bearing **(i,k)** brain samples. **(h,j)** 3D render zoom-ins of deep micro-vasculature: tumor blood vessels (GBM mV) appear aberrant, while healthy ones (mV) more orderly.

Imaging MRT irradiation

After imaging healthy and cancerous brain micro-morphology, we investigated PCI's ability to visualize fractionated radiation effects on nervous tissue, with results summarized in Fig. 4 (data from samples 2-4, 5 and 8). Brain samples from MRT-treated animals bear the typical signatures of this radiosurgery methodology: the spatially-fractionated high-dose microbeams mark brain tissue with 50 µm parallel lines of tissue ablation, interspersed by valley regions of low dose delivery. Hypo-dense (and thus hypo-intense in PCI) comb-like patterns are visible in *post-mortem* PCI images (Fig. 4a-e) and were confirmed by comparison to histology (Fig. 4a'-e' vs. 4a''-e''). Finally, the ablations were related to similar patterns appearing also in MRI images (Fig. 6).

Via PCI, different modes of irradiation can be recognized, differentiated and verified post-treatment: cross-firing modes (Fig. 4b and 4d) feature a checkered irradiation signature, as opposed to the striated patterns typical of unidirectional treatment (Fig. 4a, 4c, 4e). Post-irradiation tumor growth and *post-mortem* sample preparation play a role in making the micrometric hypo-dense striations appear only quasi-parallel or even curved. Still, relative spacing in-between ablations is preserved. Radiation-driven tissue ablations are likewise detected by PCI as they target cancerous masses (Fig. 4c, 4d). We observe MRT beam-paths transect distorted hippocampal cell layers, hyperplastic vessels (Fig. 4c, 4c'), or cortical brain tissue (Fig. 4d, 4d') and hit implanted tumors, which are calcifying, present extravasations (Fig. 4c), or are infiltrating adjacent regions (Fig. 4d). Microbeams slice the target region into parallel micro-planes, and blood vessels within nervous tissue are also traversed by the radiation. Despite the high doses delivered (> 250 Gy), we observe preservation of vascular anatomic continuity post-treatment of both large and microscopic vessels: vasculature can be followed branching across microbeam-ablated areas, resist microbeam erosion and connect to valley-dose tissue regions (Fig. 4e, 4e'). By comparison to H&E histology, microbeams appear well resolved by PCI within the layers of denser cellularity and with abundant cell bodies, such as the cerebellar granular layer (Fig. 4a'-a''), areas within the cortex and midbrain regions (Fig. 4b', 4b'') or the packed pyramidal and granular layers of the hippocampus (Fig. 4c', 4c''). Less image contrast is achieved when the ablations cross the cerebellar molecular layer and white matter regions (Fig. 4a'-a''), or the sparser-in-cell-bodies and more fiber-rich hippocampal strata (Fig. 4c', 4c''), though a glimpse of their presence and directionality can be in most cases still recognized by the expert eye. Signs of intra-microbeam reactive gliosis are revealed by GFAP (Fig. 4d'') and compared to PCI (Fig. 4d'): in both panels we observe right hemispheres with crossed microbeam paths, and contralateral hemispheres with unidirectional microbeams. Additionally, Iba-1 immunohistochemistry in **Suppl. Fig. 10** shows signs of microglial infiltration (Iba-1-positive cells) along microbeam paths. Finally, the preserved morphology of MRT-targeted local vasculature and microvasculature recognized by PCI was confirmed by comparison to H&E histology in Fig. 4e'-4e''.

Figure 4| Phase-contrast CT of MRT treatment on normal tissue, tumor tissue and vessels. 1.5 months after irradiation collimated X-ray planes administered during MRT treatment appear on brain tissue as comb-like traces of tissue ablation. Red arrows point in the direction of incoming microbeams (width 50 µm). Coronal slices of: **(a)** unidirectional MRT irradiation with peak entrance-dose at 400 Gy and 200 µm c-t-c inter-microbeam distance. Zoom-in of microbeam ablations within cerebellar granular (gr) and molecular (mo) layers, and the *arbor vitae*, resolved by PCI **(a')** and confirmed by H&E histology **(a'')**. **(b)** cross-firing MRT irradiation at 2x400 Gy and 400 µm c-t-c distance. **(b'')** histology confirms presence of the checkered ablations seen via PCI **(b')** in both the cortex (CTX) and midbrain regions (MB). **(c)** unidirectional MRT irradiation, with peak entrance-dose at 600 Gy and 200 µm c-t-c inter-microbeam distance, crossing inner layers of a dorsal hippocampus (HIP) distorted by nearby tumor growth. Presence of local high-Z material accumulation is observed (cal/fe, confirmed as calcium and iron deposits in Fig. 5), and vasculature shows signs of tumor-induced endothelial-cell hyperplasia (hyp). MRT- driven transection of hippocampal layers is detected by PCI **(c')** and confirmed by H&E histology **(c'')**. MRT ablation contrast is relatively strong in pyramidal (pyr) and granular (gr) layers, feebler in the other layers. **(d)** cross-firing MRT irradiation at 400x2 Gy and 200 µm c-t-c distance crossing the brain cortex (CTX) and targeting a glioblastoma tumor (GBM) in the lateral ventricle, showing microscopic cancerous infiltration (inf) toward the diencephalon. Intra-microbeam cells are positive for GFAP immunostaining **(d'')**, revealing signs of reactive gliosis along beam paths, which are visible in both PCI **(d')** and GFAP **(d'')** as crossed ablations in the right brain hemisphere, and as feeble uni-directional ones in the contralateral hemisphere further away from incoming MRT radiation. **(e, e')** brain vasculature and microvasculature (vas and µvas, in turquoise) resist microbeam erosion, bridging across microbeam-generated gaps, as confirmed by histology **(e'')**.

PCI-CT & Histology

PCI as an anatomical neuroimaging modality was compared to histology and to immunohistochemistry in Fig. 5, by analyzing a brain sample featuring a GBM tumor growing in the striatum, in the lateral ventricle and massively infiltrating the nearby thalamus (data from sample 6). Overall, as already observed in Figures 1 to 4, here too PCI image contrast (Fig. 5a-a'-a'') matches the morphological histology of normal and tumor tissues afforded by both H&E stain (Fig. 5b-b’-b’’) and Nissl stain (Fig. 5c-c’). MRT-driven ablations are also visible via all three techniques (Fig. 5a,b,c). Broad pathologic hyper-intense regions in PCI, attributed to GBM cancerous tissues already in Fig. 2, are visible in the PCI coronal slice in Fig. 5a. Again, GBM hyper-intense signal and altered morphology in PCI finds histological match in the signal and morphology of the most strongly marked tissues of both Nissl and H&E histology data (Fig. 5a,a’’ vs. 5b,b’’ and 5c,c’): denser and altered GBM cancerous cellularity seen via histology (5b’’, 5c’) leads to macroscopic tumor-driven morphological tissue modifications and to cellular hyper-density, both of which increase PCI signal (5a’’). Normal striatal tissue cellularity (5b’), in comparison, leads to a lower more homogeneous PCI signal (5a’). Though the cellular level reached via histology is not fully resolved in PCI at this imaging resolution, we observe once again how tissue cellular micro-milieu and macroscopic morphological differences between normal and cancerous tissues together play an important role in determining PCI signal differences.

Immunohistochemical analysis (Fig. 5d-f) of GFAP, a marker of reactive gliosis, Iba-1, a microgliosis marker, and Ki-67 protein, a marker of proliferating cells, shows the altered cellularity in the tumor mass detected via PCI, and additionally allows the identification of different cellular types in the tumor. Analysis of GFAP (Fig. 5d, 5d’) shows the presence of reactive astrocytes within cancerous tissues, and few reactive astrocytes also along MRT microbeam paths (see MRT tissue ablations and immunohistochemistry also in Fig. 4d’-d’’). Analysis of Iba-1 (Fig. 5e, 5e’) shows the presence of a massive microglial inflammatory infiltration within cancerous tissues, and very few microglial cells along MRT microbeam paths. Finally, analysis of the expression of the Ki-67 protein (Fig. 5f, 5f’) shows the presence of dividing cells within cancerous tissues only.

Next, PCI images of MRT-treated tumor-bearing samples were often observed to present areas of bright globular agglomerates (Fig. 5g) within and surrounding tumor tissues. Due to image windowing, these ultra-dense areas (most likely pertaining to an absorbing high-Z material) appear as extended bright saturated patches in PCI (Fig 5g’), though they are actually grainy in morphology, as visible when gray-levels are better adjusted to visualize these features alone (Fig. 5g’’). In Fig. 5h-h’, obtained by multiplication of 5g’ and the inverse of 5g’’, we can create artificial intra-agglomerate image contrast, which enables the visualization of the correct agglomerate local morphology via PCI. In fact, by substituting to the original image the ultra-dense patches in Fig. 5g'', this time with inverted pixel gray-levels, we form central dark/black ultra-dense clusters, which highlight the proper local shape of the ultra-bright region in the original unaltered PCI image in Fig. 5g. Histological analysis characterized the ultra-dense PCI-detected features in Fig. 5g-h as regions of altered cellular composition (Fig. i,i'), where accumulation of calcium (Fig. 5j,j') and iron deposits (Fig. 5k,k') is present. In fact, the ultra-dense agglomerates in PCI (dark pixels in Fig. 5h) correspond to large areas of altered tissue cellularity and possible calcification in H&E histology (Fig. 5i). Moreover, these same areas are positive to Alizarin red S staining (Fig. 5j), specific for calcium deposits, and to Perls' Prussian Blue staining (Fig. 5k), specific for the detection of iron. The broad shapes of the deposits are closely matching in all four methodologies (Fig. h-i-j-k). Moreover, by zooming in and viewing the agglomerates at the supra-cellular level (Fig. h'-I'-j'-k'), we observe how the deposits are composed of many localized round grains in both PCI (Fig. 5h', dark/black grains), H&E histology (Fig. 5i', dark-pink grains), after Alizarin red S staining (Fig. 5j', red grains) and after Perls' Prussian Blue staining (Fig. 5k'). Again the methods all afford similar morphological results and complement each other in terms of functional information. The presence of calcium and iron accumulation within degenerating cancerous tissues, either radiation-induced, as already reported in literature[70–72], or from intra-tumor calcification or blood extravasation, leads to very intense bright signals in PCI. We can conclude that highly dense materials (such as iron and calcium) strongly affect PCI imaging and could be involved in the formation of the PCI signal hyper-intensities observed within vasculature (from iron-rich blood aggregates) or within GBM tissues (again from the high blood volumes likely present). These results, supported by the immunohistochemistry in Fig. 5, are in line with the characterization of both GBM and vasculature morphology made in Fig. 2 and 3. Full histological and immunohistochemical datasets are included in **Suppl. Fig. 10**.

Figure 5| Histological and immunohistochemical confirmation of X-ray phase-contrast CT imaging. **(a)** Coronal PCI at the -2.4 mm from bregma level of a rat brain bearing a GBM. **(b)** Corresponding hematoxylin/eosin (H&E) staining at the same bregma level. **(c)** Coronal Nissl staining at the -2.5 mm from bregma level of a rat brain bearing a GBM. **(d)** Immunohistochemistry for GFAP of an adjacent coronal section of a rat bearing GBM. Note the presence of GFAP-positive cells in the tumor tissues and along MRT microbeam paths. **(e)** Immunohistochemistry for Iba-1 in an adjacent coronal section of a rat bearing GBM. Note the presence of Iba-1-positive cells in the tumor tissues and along MRT microbeam paths. **(f)** Immunohistochemistry for Ki-67 in an adjacent coronal section of a rat bearing GBM. Note the presence of Ki-67-positive cells in the tumor tissues. **(a', b')** Details of PCI and H&E staining taken in the normal contralateral striatum, showing respectively smooth local morphology and normally-appearing cells. **(a'', b'')** Details of PCI and H&E staining taken within GBM tissue, showing respectively altered morphology and cancer cells. **(c')** Higher magnification of Nissl staining taken within GBM tissue, showing altered cellularity. **(d')** Higher magnification of GFAP-positive cells taken within GBM tissue. **(e')** Higher magnification of Iba-1-positive cells taken within GBM tissue. **(f')** Higher magnification of K-67-positive cells taken within GBM tissue. **(g)** Coronal PCI at the -4.8 mm from bregma level of a rat brain bearing a GBM, showing an extended area of accumulation of bright high-Z material (cal/fe) within cancerous tissue in **(g')**. **(g'')** readjusted image windowing of **(g')** to show the grainy morphology of the high-Z material accumulations. **(h)** PCI Zoom-in obtained by multiplication of **(g')** and the inverse of **(g'')**. The artificial gray-levels enable the visualization of correct agglomerate local morphology. Note the *sui generis* meaning of the inverted dark pixels in **(h)** after the image processing, unconventionally standing for ultra-density instead of for low-density. **(h')** Magnification of **(h)**: note the granular morphology of the ultra-dense particles (arrows in **h')**. **(i, i')** Different magnifications of H&E histology show calcifications within altered cancerous tissue corresponding to the hyper-dense agglomeration area in **(h, h')** and **(g)**. These calcifications (large dark pink grains, arrows in **i'**) appear as areas of high-intensity signal in (**g'-g''-h**) as a likely result of tumor-driven tissue degeneration. (**j,j'**) Different magnifications of Alizarin Red S staining, specific for calcium deposits, within the tissue corresponding to the PCI image in **(h)**. Note the granular morphology of the red-stained particles (arrow in **j')**. (**k,k'**) Different magnifications of Perls' Prussian Blue staining, specific for iron deposits, within the tissue corresponding to the PCI image in **(h)**. Note the granular morphology of the blue-stained particles (arrow in **k'**).

PCI-CT & MRI

Various both T1- and T2-weighted ultra-high-field 9.4 T MRI measurements were performed on one brain sample (sample 1), and compared to the X-ray PCI-CT datasets. The MRI sequences, optimized for high-resolution brain anatomical imaging, were selected to serve as an additional established basis for the validation of PCI as a morphological neuroimaging technique. Selected best results are included in Figure 6 (with sequence specifications in the Methods), and a complete dataset, showing the comparison of PCI signal to 10 different MRI sequences and related sequence specifications, can be found in **Suppl. Fig. 11** (axial images) and **Suppl. Fig. 12** (coronal images). As a note, the sample faced long-term storage immersed in formalin. As previously reported in literature[73], formalin fixation permanently alters relaxation and diffusion properties of CNS tissues, with resulting both T1 and T2 times being reduced with respect to standard fresh unfixed slices or compared to *in-vivo* imaging. In fact, the measured T1 and T2 maps (**Suppl. Fig. 13)** show reduced T1/T2 times compared to standard literature values (**Suppl. Table 1** and **Suppl. Table 2**). In light of this, the MRI data presented here (Fig. 6), though it can still serve as an established platform for the validation of PCI neuro-contrast, it is not appropriate for a quantitative contrast comparison, which would need specific *ex-vivo* MRI sample fixation, washing and staining procedures[10] in order to fully exploit the technique's potential.

Full-organ gross brain anatomical features are visible in axial images from both T1-weighted (Fig. 6a) and T2-weighted (Fig. 6b) MRI. Furthermore, we observe that the corresponding PCI-CT dataset slice (Fig. 6c) renders a matching sample brain local morphology, for example, in the layers of hippocampal tissue, in brain ventricles, in the striatum region and for large fiber tracts. The DTI metric D_{ZZ} tensor symmetric component (a diffusion map) and RARE imaging (Fig. 6d-e) both show high fiber-tract contrast (forebrain bundles especially) compared to corresponding PCI-CT (Fig. 6f), which instead seems more sensitive to the densely-packed micro-environment of neuron cell-bodies in the hippocampal pyramidal and granular layers. MSME (Fig. 6a), MGE (Fig. 6g), FLASH (Fig. 6b) and RARE (Fig. 6e,h) sequences all detect the microbeam-induced tissue ablations visible in PCI-CT images (Fig. 6c,f,i). Microbeams appear as hyper-intense parallel lines in the MSME and FLASH scans, and instead as hypo-intense in both MGE and RARE maps. MRT tissue ablations feature local hypo-density, and thus appear hypo-intense in PCI maps, as already shown in Fig. 4. Both imaging techniques well describe intra-cerebral calcifications and iron deposits (see also Fig. 5), which are hypo-intense in MRI and hyper-intense in PCI-CT (Fig. 6a,b vs. 6c and 6d,e vs. 6f). Finally, overall tumor morphology can be appreciated in both imaging modalities (Fig. 6a vs. 6c, and 6e vs. 6f). PCI-CT's higher resolution benefits the visualization of local intra-tumor details from pathological GBM cellularity and vasculature (Fig. 6c,f).

Figure 6| X-ray phase contrast CT vs. MRI.

Corresponding axial images of a tumor-bearing MRT-irradiated brain, from **(a)** a T2-weighted MSME sequence, **(b)** a T1-weighted FLASH sequence and **(c)** PCI-CT, compare local anatomy of the hippocampus (HIP), lateral ventricles (LV), striatum (STR) and cerebral fiber tracts (FTr). Corresponding coronal images of the same sample, at a first slice-level from **(d)** the DTI metric D_{zz} symmetric tensor component (a diffusion image), **(e)** a T1-weighted RARE sequence and **(f)** PCI-CT, and at a second slice-level from **(g)** a T2*-weighted MGE sequence, **(h)** a T1-weighted RARE sequence and **(i)** PCI-CT: medial forebrain bundles of fiber tracts (mFTr) show strong RARE signal **(e)** and some diffusion signal in the D_{zz} DTI metric **(d)**, whereas lateral forebrain bundles (lFTr) are visible also in PCI-CT **(f)**; pyramidal (pyr) and granular (gr) layers of the hippocampus in **(f)** can be resolved at high resolution. Finally, both MRI and PCI images show sensitivity to deposits of iron and calcium (cal/fe), to MRT-induced tissue ablations (MRT) and to glioblastoma tissue (GBM) **(a-i)**. Red arrows point in the direction of incoming microbeams.

Discussion:

This experimental neuroimaging study evaluates how well PCI-CT imaging can visualize the effects of MRT on normal and tumor tissue in the brain of an animal model. Our results show micrometric histological precision and high soft-tissue contrast without addition of contrast agent (Fig.1-4, Suppl. Fig. 7), enabling effective 3D full-organ segmentations and renderings of complex anatomical and pathological brain structure (Fig. 2, Suppl. Fig. 9).

Being sensitive to the refraction of X-rays in matter, PCI-CT is particularly adapted to visualize weakly absorbing details, like those often encountered in biology and medicine. In fact, this imaging method has already been demonstrated to enable the *ex-vivo* analysis of a broad range of biological tissues, and has been recognized as interesting for biomedical applications and experimental studies[33]. Of note in the result presented in this work is the variety of concurrent anatomical detail PCI is sensitive to: intra-cortical micro-vasculature and cancerous lesions are well depicted alongside MRT-driven tissue ablations and minute cerebral structures, such as the dentate gyrus within the dorsal hippocampus or the choroid plexi within lateral ventricles (Fig. 1-3). Moreover, worth mentioning, and of interest to preclinical studies, beyond a delineation of *ex-vivo* CNS gross anatomy comparable to that of MRI (Fig. 6), is the achievable degree of precision in the rendering of brain and brain tumor micro-anatomy, even after sample storage in formalin fixative. For example, phase-contrast within several neuronal microscopic strata, such as the pyramidal and granular layers of the hippocampal formation, was observed both in healthy layers and after transection by MRT radiation (Fig. 1e, Fig. 4c'). Micrometric striated tissue ablations, traced by high-dose parallel X-ray microbeams, forming comb-like hypo-dense patterns, were visible via PCI imaging also in cerebellar and cerebral regions of the brain organ (Fig. 3). Last, we observed diverse of local tissue effects due to both MRT treatment and GBM tumor growth, from pseudopalisading (Fig. 2e) and to necrosis (Fig. 2c,e), to intra-tumor deposition of iron and calcium granular aggregates (Fig. 2e, Fig. 4c, Fig. 5g-h-h') and to tumor infiltration (Fig. 4d and 5).

As already mentioned, in terms of contrast mechanism, the X-ray PCI-CT technique exploits the phase effects of an X-ray wave within a material[49], a process governed by its index of refraction. In simple terms, the technique produces a 3D spatial distribution of phase shifts, which depend on local material properties including the local electronic density. Macroscopically, this signal can be understood as a map of the local density and refraction-related properties of a material, with PCI image contrast arising from local relative differences in these properties. This fact holds true also for biological materials, such as the nervous tissue in the brain, where absorption effects are generally quite small. High PCI contrast can be observed in Fig.1, for example, between the two (granular and molecular) layers of gray matter in the cerebellum (Fig. 1a, 1d). The granular layer contains a high number of small but densely-packed neuron cells (granule cells) and is reported to make up a disproportionate amount of the brain's mass compared to its volume, thus forming a peculiarly dense layer[74]. Instead, the cells present in the nearby molecular layer, are much sparser. This difference in cellular composition is well-described by H&E-stained histological cerebellar slices, where the abundant cell-bodies in the granular layer stain dark violet (hematoxylin attaches to intra-soma DNA/RNA), whereas the molecular layer, where fewer cell nuclei are present, stains mainly pink (from the eosin). Interestingly, the two layers show distinctly different PCI signals (see Fig. 1a and 1d, labeled *mo* and *gr*) and give rise to high phase-contrast. MRI contrast between granular and molecular layers, instead, is reported[39] to be low, suggesting that similar tissue environments for water molecules and low differences in local vasculature and blood volumes are present. Since the key tissue feature discriminating between the cerebellar gray matter layers is the difference in cellular density and composition (and thus of tissue cellularity, intended as number and type of cells present), the observed high PCI contrast within these layers points toward a link between PCI signal and local brain tissue cellularity. This connection seems to hold also in the white matter layer of the cerebellum. Central to the granular layer and formed mainly by input and output nerve-fiber systems, it is also poor in cell somas (being mainly composed of climbing and mossy fibers) and it typically stains mostly pink in H&E histology. As expected from its cellularity (low cell-soma densities), its PCI signal (see Fig. 1d, labeled *arb*) is also relatively hypo-intense relatively to the granular layer. Finally, the same relationship can also be seen in the granular vs. molecular layers of the hippocampus in Figures 1e-f-g: the H&E histology stains the granular layer mostly violet and the molecular layer mostly pink (Fig. 1f), highlighting cellularity differences. And the PCI too exhibits hyper-intensity in the granular layer compared to the molecular one (Fig. 1e). Several other figure panels (in Fig. 2, 4 and 5) compare brain tissue cellularity highlighted by H&E staining to corresponding PCI contrast. What we observe overall is a representation of local brain morphology (how tissue shapes are visualized), which is quite similar in both techniques (PCI vs. H&E). Moreover, histological cellular staining levels seem to relate to PCI signal intensities as well (with areas of hyper-intense PCI matching histological areas of hyper-cellularity). In light of the type of PCI contrast observed in all these tissues, a link between PCI signal and local tissue cellularity seems plausible to us. Moreover, this link seems reasonable, because for biological tissues it is their composition (and thus also their cellularity) that influences local density and refractive properties, and thus PCI measurements.

A similar relationship between overall tissue composition, cellularity and PCI contrast should hold also in the case of GBM tissue. At the cellular level, the abnormal biology of GBM tissue, e.g. local parenchymal destruction, hyper-cellularity, metastatic cell infiltration, high-rates of cell reactive gliosis, proliferation, high blood local volumes, aberrant hyperplastic microvasculature as well as blood extravasation are all factors, which concur to generate densely-packed, blood-rich and chaotic intra-tumoral environments. This exotic tissue micro-milieu must influence local density and refraction properties, and thus should reasonably also play a role in PCI contrast formation. In panels 2f-g, 2h-i-j, and even 2e-e', we observe GBM tissues, which stain dark-violet in H&E histology. PCI shows GBM tissues, which morphologically follow the histological GBM shapes, and an overall local increase in PCI signal in all datasets acquired (Fig. 2a and 2b). In addition, PCI-based panels 3i-j-k showcase the rich presence of local aberrant GBM vasculature and micro-vasculature. Overall, the imaging method seems to provide cancer-tissue morphological visualizations that are related to local malignant cellularity and to malignant tissue and vasculature anatomy. And, in light of the PCI contrast mechanism already noted for normal brain layers, the observed link between PCI hyper-signal, GBM density, hyper-cellularity, high blood contents and local aberrant micro-vasculature does indeed seem reasonable. This biological interpretation of the detected PCI signal seems also supported by the immunohistochemical analysis in Fig. 3 and 5. Admittedly, though, PCI is a morphological experimental imaging modality but not a functional imaging tool, and for this reason any differentiation of brain structure based on PCI intensity information should best be complemented at least partially by the recognition of specific morphological features.

As already discussed, other cutting-edge technologies used in neuroimaging have their strengths and limits: brain micro-MRI can routinely be applied *in-vivo* at increasing resolution for both morphological and functional imaging, but for the highest *ex-vivo* resolutions needs tailored 'staining' protocols and struggles to achievable sub-micrometric resolution. Most other high-resolution preclinical neuroimaging techniques instead can clearly observe cellular and subcellular detail, but offer only a partial or localized (often stain-dependent) anatomical visualization, including traditional 2D imaging approaches like histology or scanning electron microscopy. To the best of our knowledge, PCI is the only imaging technique providing rodent full-organ micrometric resolution in neuroimaging and high-contrast tumor imaging without extensive sample-preparation (e.g. without injection of intra-venous contrast, mechanical alterations or dissection). For its part, a current clear limitation of PCI-CT in neuroimaging is the difficulty arising when the method is applied *in-vivo* in the CNS: the negative influence of high-scattering and porous materials, such as those within the skull and vertebral bones, on the detectable X-ray phase-contrast drastically reduces the quality of intra-skull and intra-vertebral nervous tissue visualizations. PCI resolution limits are related to detector, optics and X-ray source technologies, and ongoing technological efforts aim to obtain even sub-micron resolution datasets (i.e. cellular level datasets) at fields-of-view interesting for brain soft-tissue small animal studies. Other limitations for *in-vivo* experimental applications are due to the high doses delivered in CT mode in combination with motion-artifact reduction algorithms, and to the high current acquisition times needed by laboratory setups, where the available photon fluxes are much lower compared to those available at synchrotron sources. Ongoing new developments in both dose-reduction algorithms[36] and compact high-flux X-ray light sources[75] are aimed at mitigating these challenges. Moreover, PCI-CT today can be applied also in the laboratory with several novel advanced X-ray-tube technologies[76–78], freeing this imaging technique from a synchrotron-only setting.

The results presented here explore a young and challenging field of application for PCI, experimental neuroimaging. Though a full biological and functional characterization in many cases will still necessitate immunohistochemical analysis, the methods used here appear well-suited for *post-mortem* morphological brain analyses, which need to avoid any sample dissection. In fact, complex full-organ vascular and cancerous pathologies arising from GBM tumor were visualized within an excised rodent encephalon. Moreover, the morphology of biological and physical effects on nervous tissue after brain cancer radiotherapy were also faithfully depicted. The microbeam configuration, geometry and dose distributions used within this study (peak and valley doses, microbeam size, center-to-center distances and irradiation area) are all in line with the values used in the literature of MRT preclinical research on rodents[79–82]. In addition, following published Monte Carlo calculations, the doses used are relevant also in view of the clinical translation of MRT[60]. In light of this, the presented results, by setting the groundwork for the identification of GBM tissue, of MRT-driven tissue ablations and of both normal and pathologic vascularization, can serve as a guide for image interpretation of future PCI-based *ex-vivo* imaging studies of MRT treatment using standard irradiation parameters. Tumor radio-resistance and drug efficacy studies could also benefit from the volumetric quantifications of tissue volume modifications, which PCI can provide. Finally, and most importantly, this manuscript shows how the PCI technique can precede and guide localized histological analyses (e.g. immunohistochemistry, as shown in Fig. 5), and how it can be used for multimodal biomedical imaging in combination with, before or after other experimental neuroimaging methodologies (e.g. before MRI, as shown in Fig. 6).

Conclusions:

Our results demonstrate that PCI-CT is an experimental imaging technique viable for *ex-vivo* follow-up studies of X-ray radiotherapy techniques, e.g. MRT, on small animal models. In fact, PCI-CT, sensitive to soft tissue morphology and composition, provided high-contrast microscale representations of 3D full-organ rodent brain anatomy. PCI images concurrently visualized deep encephalic tumor tissues, healthy tissues, micrometric angio-structure and the effects of high-dose ionizing radiation, all within a one-shot image and without the need to dissect the sample. Moreover, PCI-CT signals were shown to match histological and immunohistochemical data, and to find a counterpart also in experimental high-field MRI. In conclusion, the deep insight into brain and cancer anatomy, which this imaging technique was able to provide *ex-vivo*, make it an interesting tool for neurological studies. PCI-based morphological representations of complex vascular and cancerous pathologies, and of biological effects after brain cancer radiotherapy could provide new insight, among others, to studies on local brain tumor tissue radio-resistance, or on drug efficacy in experimental models of neurodegeneration. This technique can precede and guide histological analysis, and can be used for multimodal biomedical imaging in combination with or after other experimental neuroimaging methodologies.

References:

1. Girst S, Greubel C, Reindl J, et al. Proton Minibeam Radiation Therapy Reduces

Side Effects in an in Vivo Mouse Ear Model. *Int J Radiat Oncol Biol Phys*. 2016;95(1):234-241. doi:10.1016/j.ijrobp.2015.10.020.

2. Smyth LML, Senthi S, Crosbie JC, Rogers PAW. The normal tissue effects of microbeam radiotherapy : What do we know , and what do we need to know to plan a human clinical trial? *Int J Radiat Biol*. 2016;92(6):302-311. doi:10.3109/09553002.2016.1154217.
3. Bräuer-Krisch E, Serduc R, Siegbahn EA, et al. Effects of pulsed, spatially fractionated, microscopic synchrotron X-ray beams on normal and tumoral brain tissue. *Mutat Res - Rev Mutat Res*. 2010;704(1-3):160-166. doi:10.1016/j.mrrev.2009.12.003.
4. Dilmanian FA, Morris GM, Zhong N, et al. Murine EMT-6 carcinoma: high therapeutic efficacy of microbeam radiation therapy. *Radiat Res*. 2003;159(5):632-641. doi:10.1667/0033-7587(2003)159[0632:MECHTE]2.0.CO;2.
5. Bouchet A, Lemasson B, Le Duc G, et al. Preferential effect of synchrotron microbeam radiation therapy on intracerebral 9l gliosarcoma vascular networks. *Int J Radiat Oncol Biol Phys*. 2010;78(5):1503-1512. doi:10.1016/j.ijrobp.2010.06.021.
6. Sabatasso S, Laissue JA, Hlushchuk R, et al. Microbeam radiation-induced tissue damage depends on the stage of vascular maturation. *Int J Radiat Oncol Biol Phys*. 2011;80(5):1522-1532. doi:10.1016/j.ijrobp.2011.03.018.
7. Benveniste H, Blackband S. MR microscopy and high resolution small animal MRI: Applications in neuroscience research. *Prog Neurobiol*. 2002;67(5):393-420. doi:10.1016/S0301-0082(02)00020-5.
8. Lin CY, Siow TY, Lin MH, et al. Visualization of rodent brain tumor angiogenesis and effects of antiangiogenic treatment using 3D ΔR2-μRA. *Angiogenesis*. 2013;16(4):785-793. doi:10.1007/s10456-013-9355-8.
9. Engelhorn T, Eyupoglu IY, Schwarz MA, et al. In vivo micro-CT imaging of rat brain glioma: A comparison with 3 T MRI and histology. *Neurosci Lett*. 2009;458(1):28-31. doi:10.1016/j.neulet.2009.04.033.
10. Johnson GA, Cofer GP, Gewalt SL, Hedlund LW. Morphologic Phenotyping with MR Microscopy: The Visible Mouse. *Radiology*. 2002;222:789-793.

11. Chuang N, Mori S, Yamamoto A, et al. An MRI-based Atlas and Database of the Developing Mouse Brain. *Neuroimage*. 2011;54(1):80-89. doi:10.1016/j.neuroimage.2010.07.043.An.
12. Johnson GA, Calabrese E, Badea A, Paxinos G, Watson C. A Multidimensional Magnetic Resonance Histology Atlas of the Wistar Rat Brain. 2012;62(3):1848-1856. doi:10.1016/j.neuroimage.2012.05.041.A.
13. Calabrese E, Badea A, Watson C, Johnson GA. A quantitative magnetic resonance histology atlas of postnatal rat brain development with regional estimates of growth and variability. *Neuroimage*. 2013;71:196-206.
14. Mukherjee P, Berman JI, Hess CP, Henry RG. Diffusion Tensor MR Imaging and Fiber Tractography : Theoretic Underpinnings. *AJNR*. 2008. doi:10.3174/ajnr.A1051.
15. Veraart J, Leergaard TB, Antonsen BT, et al. Population-averaged diffusion tensor imaging atlas of the Sprague Dawley rat brain. *Neuroimage*. 2011;58:975-983. doi:10.1016/j.neuroimage.2011.06.063.
16. Jiang Y, Johnson GA. Microscopic diffusion tensor atlas of the mouse brain. *Neuroimage*. 2011;56:1235-1243. doi:10.1016/j.neuroimage.2011.03.031.
17. Shepherd TM, Ozarslan E, Yachnis AT, King MA, Blackband SJ. Diffusion Tensor Microscopy Indicates the Cytoarchitectural Basis for Diffusion Anisotropy in the Human Hippocampus. *Am J Neuroradiol*. 2007;28:958-964.
18. Chenevert TL, Lauren D, Taylor JMG, et al. Diffusion Magnetic Resonance Imaging : an Early Surrogate Marker of Therapeutic Efficacy in Brain Tumors. *Jourmal Natl Cancer Inst*. 2000;92(24):2029-2036. doi:10.1093/jnci/92.24.2029.
19. Bennett KM, Hyde JS, Rand SD, et al. Intravoxel Distribution of DWI Decay Rates Reveals C6 Glioma Invasion in Rat Brain. 2004;1004:994-1004. doi:10.1002/mrm.20286.
20. Kim E, Zhang J, Hong K, Benoit NE, Pathak AP. Vascular phenotyping of brain tumors using magnetic resonance microscopy (µMRI). *J Cereb Blood Flow Metab*. 2011;31:1623-1636. doi:10.1038/jcbfm.2011.17.
21. Virdee K, Cumming P, Caprioli D, et al. Applications of positron emission tomography in animal models of neurological and neuropsychiatric disorders.

Neurosci Biobehav Rev. 2012;36(4):1188-1216. doi:10.1016/j.neubiorev.2012.01.009.

22. Song A, Charles AS, Koay SA, et al. Volumetric two-photon imaging of neurons using stereoscopy (vTwINS). *Nat Methods*. 2017;14(4). doi:10.1038/nmeth.4226.
23. Birkner A, Tischbirek CH, Konnerth A. Improved deep two-photon calcium imaging in vivo. *Cell Calcium*. 2016:1-7. doi:10.1016/j.ceca.2016.12.005.
24. Yashiro H, Nakahara I, Funabiki K, Riquimaroux H. Micro-endoscopic system for functional assessment of neural circuits in deep brain regions: Simultaneous optical and electrical recordings of auditory responses in mouse's inferior colliculus. *Neurosci Res*. 2017:1-9. doi:10.1016/j.neures.2017.01.002.
25. Bouvier DS, Jones E V, Quesseveur G, et al. High Resolution Dissection of Reactive Glial Nets in Alzheimer ' s Disease. *Sci Rep*. 2016;(6):24544. doi:10.1038/srep24544.
26. Hama H, Hioki H, Namiki K, et al. Sca/eS : an optical clearing palette for biological imaging. *Nat Neurosci*. 2015;18(10):1518-1529. doi:10.1038/nn.4107.
27. Ertürk A, Mauch CP, Hellal F, et al. Three-dimensional imaging of the unsectioned adult spinal cord to assess axon regeneration and glial responses after injury. *Nat Med*. 2012;18(1):166-172. doi:10.1038/nm.2600.
28. Pan C, Cai R, Quacquarelli FP, et al. Shrinkage-mediated imaging of entire organs and organisms using uDISCO. *Nat Methods*. 2016;13:859-867. doi:10.1038/nmeth.3964.
29. Tearney GJ, Brezinski ME, Bouma BE, et al. In Vivo Endoscopic Optical Biopsy with Optical Coherence Tomography. *Science (80-)*. 1997;276(June):2037-2040.
30. Xie Y, Bonin T, Loffler S, Huttmann G, Tronnier V, Hofmann UG. Coronal in vivo forward-imaging of rat brain morphology with an ultra-small optical coherence tomography fiber probe. *Phys Med Biol*. 2013;58:555-568. doi:10.1088/0031-9155/58/3/555.
31. Xie Y, Martini N, Hassler C, et al. In vivo monitoring of glial scar proliferation on chronically implanted neural electrodes by fiber optical coherence tomography. *Front Neuroeng*. 2014;7(34). doi:10.3389/fneng.2014.00034.
32. Chen W, You J, Gu X, Du C, Pan Y. High-speed swept source optical coherence

Doppler tomography for deep brain microvascular imaging. *Sci Rep*. 2016;6:38786. doi:10.1038/srep38786.

33. Bravin A, Coan P, Suortti P. X-ray phase-contrast imaging: from pre-clinical applications towards clinics. *Phys Med Biol*. 2013;58(1):R1-R35. doi:10.1088/0031-9155/58/1/R1.
34. Sztrókay A, Diemoz PC, Schlossbauer T, et al. High-resolution breast tomography at high energy: a feasibility study of phase contrast imaging on a whole breast. *Phys Med Biol*. 2012;57(10):2931-2942. doi:10.1088/0031-9155/57/10/2931.
35. Donath T, Pfeiffer F, Bunk O, et al. Toward clinical X-ray phase-contrast CT: demonstration of enhanced soft-tissue contrast in human specimen. *Invest Radiol*. 2010;45(7):445-452. doi:10.1097/RLI.0b013e3181e21866.
36. Zhao Y, Brun E, Coan P, et al. High resolution, low-dose phase contrast x-ray tomography for 3D diagnosis of human breast cancers. *Proc Natl Acad Sci U S A*. 2012;109(45):18290-18294. doi:10.1073/pnas.1204460109/-/DCSupplemental.www.pnas.org/cgi/doi/10.1073/pnas.1204460109.
37. Horng A, Brun E, Mittone A, et al. Cartilage and Soft Tissue Imaging Using X-rays: Propagation-Based Phase-Contrast Computed Tomography of the Human Knee in Comparison With Clinical Imaging Techniques and Histology. *Invest Radiol*. 2014;49(9):627-634. doi:10.1097/RLI.0000000000000063.
38. Yoneyama A, Baba R, Hyodo K, Takeda T. Quantitative comparison of performance of absorption , Talbot interferometric , and crystal x-ray interferometric imaging. *EPOSTM, ECR*. 2015;(C-0531). doi:10.1594/recr2015/C-0531.
39. Schulz G, Waschkies C, Pfeiffer F, et al. Multimodal imaging of human cerebellum - merging X-ray phase microtomography, magnetic resonance microscopy and histology. *Sci Rep*. 2012;2:826. doi:10.1038/srep00826.
40. Pfeiffer F, Bunk O, David C, et al. High-resolution brain tumor visualization using three-dimensional x-ray phase contrast tomography. *Phys Med Biol*. 2007;52(23):6923-6930. doi:10.1088/0031-9155/52/23/010.
41. Rutishauser S, Donath T, David C, et al. A tilted grating interferometer for full vector field differential x-ray phase contrast tomography. *Opt Express*.

2011;19(25):24890-24896. doi:10.1364/OE.19.024890.

42. McDonald SA, Marone F, Hintermüller C, et al. Advanced phase-contrast imaging using a grating interferometer. *J Synchrotron Radiat*. 2009;16(4):562-572. doi:10.1107/S0909049509017920.
43. Jensen TH, Bech M, Bunk O, et al. Molecular X-ray computed tomography of myelin in a rat brain. *Neuroimage*. 2011;57(1):124-129. doi:10.1016/j.neuroimage.2011.04.013.
44. Zhang M-Q, Zhou L, Deng Q-F, et al. Ultra-high-resolution 3D digitalized imaging of the cerebral angioarchitecture in rats using synchrotron radiation. *Sci Rep*. 2015;5:14982. doi:10.1038/srep14982.
45. Beltran M a, Paganin DM, Siu KKW, et al. Interface-specific x-ray phase retrieval tomography of complex biological organs. *Phys Med Biol*. 2011;56:7353-7369. doi:10.1088/0031-9155/56/23/002.
46. Lwin T-T, Yoneyama A, Hara A, et al. Spontaneous brain tumor imaging of aged rat by crystal X-ray interferometer-based phase-contrast X-ray CT. *Acta Radiol Open*. 2016;5(2):1-6. doi:10.1177/2058460115626958.
47. Takeda T, Momose A, Hirano K, Haraoka S, Watanabe T, Itai Y. Human carcinoma: early experience with phase-contrast X-ray CT with synchrotron radiation--comparative specimen study with optical microscopy. *Radiology*. 2000;214(1):298-301. doi:10.1148/radiology.214.1.r00ja08298.
48. Huang S, Kou B, Chi Y, et al. In-line phase-contrast and grating-based phase-contrast synchrotron imaging study of brain micrometastasis of breast cancer. *Sci Rep*. 2015;5:9418. doi:10.1038/srep09418.
49. Momose A, Takeda T, Itai Y, Hirano K. Phase-contrast X-ray computed tomography for observing biological soft tissues. *Nat Med*. 1996;2(4):473-475. doi:10.1038/nm0496-473.
50. Charles-River Laboratories - France. Fischer Rat (F344/DuCrl, strain code 002).
51. Barth RF, Kaur B. Rat brain tumor models in experimental neuro-oncology: the C6, 9L, T9, RG2, F98, BT4C, RT-2 and CNS-1 gliomas. *J Neurooncol*. 2009;94(3):299-312. doi:10.1007/s11060-009-9875-7.
52. Régnard P, Bräuer-Krisch E, Troprès I, Keyriläinen J, Bravin A, Le Duc G.

Enhancement of survival of 9L gliosarcoma bearing rats following intracerebral delivery of drugs in combination with microbeam radiation therapy. *Eur J Radiol*. 2008;68(3 Supplement):151-155. doi:10.1016/j.ejrad.2008.04.049.

53. Régnard P, Le Duc G, Bräuer-Krisch E, et al. Irradiation of intracerebral 9L gliosarcoma by a single array of microplanar x-ray beams from a synchrotron : balance between curing and sparing. *Phys Med Biol*. 2008;53:861-878. doi:10.1088/0031-9155/53/4/003.
54. Mollenhauer J, Aurich ME, Zhong Z, et al. Diffraction-enhanced X-ray imaging of articular cartilage. *Osteoarthr Cartil*. 2002;10(3):163-171. doi:10.1053/joca.2001.0496.
55. Siegbahn EA, Stepanek J, Bräuer-Krisch E, Bravin A. Determination of dosimetrical quantities used in microbeam radiation therapy (MRT) with Monte Carlo simulations. *Med Phys*. 2006;33(9):3248. doi:10.1118/1.2229422.
56. Bräuer-Krisch E, Requardt H, Brochard T, et al. New technology enables high precision multislit collimators for microbeam radiation therapy. *Rev Sci Instrum*. 2009;80(74301):1-6. doi:10.1063/1.3170035.
57. Laissue JA, Blattmann H, Wagner HP, Grotzer MA, Slatnik DN. Prospects for microbeam radiation therapy of brain tumours in children to reduce neurological sequelae. *Dev Med Child Neurol*. 2007;(49):577-581.
58. Dilmanian FA, Zhong Z, Bacarian T, et al. Interlaced x-ray microplanar beams: a radiosurgery approach with clinical potential. *Proc Natl Acad Sci U S A*. 2006;103(25):9709-9714. doi:10.1073/pnas.0603567103.
59. Serduc R, Bräuer-Krisch E, Bouchet A, et al. First trial of spatial and temporal fractionations of the delivered dose using synchrotron microbeam radiation therapy. *J Synchrotron Radiat*. 2009;(16):587-590. doi:10.1107/S0909049509012485.
60. Martínez-Rovira I, Sempau J, Prezado Y. Development and commissioning of a Monte Carlo photon beam model for the forthcoming clinical trials in microbeam radiation therapy. *Med Phys*. 2012;39(1):119-131. doi:10.1118/1.3665768.
61. Cloetens P, Barrett R, Baruchel J, Guigay J-P, Schlenker M. Phase objects in synchrotron radiation hard x-ray imaging. *J Phys D Appl Phys*. 1996;29(1):133-

146. doi:10.1088/0022-3727/29/1/023.

62. Wilkins SW, Gureyev TE, Gao D-W, Pogany A, Stevenson AW. Phase-contrast imaging using polychromatic hard X-rays. *Nature*. 1996;384(6607):335-338. doi:10.1038/384335a0.
63. Bidola PM, Zanette I, Achterhold K, Holzner C, Pfeiffer F. Optimization of propagation-based phase-contrast imaging at a laboratory setup. *Opt Express*. 2015;23(23):30000-30013. doi:10.1364/OE.23.030000.
64. Coan P, Peterzol A, Fiedler S, Ponchut C, Labiche JC, Bravin A. Evaluation of imaging performance of a taper optics CCD “FReLoN” camera designed for medical imaging. *J Synchrotron Radiat*. 2006;13(3):260-270. doi:10.1107/S0909049506008983.
65. Paganin D, Mayo SC, Gureyev TE, Miller PR, Wilkins SW. Simultaneous phase and amplitude extraction from a single defocused image of a homogeneous object. *J Microsc*. 2002;206(1):33-40. doi:10.1046/j.1365-2818.2002.01010.x.
66. Lyckegaard A, Johnson G, Tafforeau P. Correction of ring artifacts in X-ray tomographic images. *Int J Tomogr Stat*. 2011;18(F11):1-9.
67. Volume Graphics GmbH. VGStudio MAX 2.2. 2001. doi:www.volumegraphics.com.
68. Rong Y, Durden DL, Meir EG Van, Brat DJ. Pseudopalisading ` Necrosis in Glioblastoma : A Familiar Morphologic Feature That Links Vascular Pathology , Hypoxia , and Angiogenesis. *J Neuropathol Exp Neurol*. 2006;65(6):529-539.
69. Siemann DW. The Unique Characteristics of Tumor Vasculature and Preclinical Evidence for its Selective Disruption by Tumor-Vascular Disrupting Agents. *Cancer Treat Rev*. 2011;37(1):63-74. doi:10.1016/j.ctrv.2010.05.001.
70. Flament-Durand J, Ketelbant-Balasse P, Maurus R, Regnier R, Spehl M. Intracerebral calcifications appearing during the course of acute lymphocytic leukemia treated with methotrexate and x-rays. *Cancer*. 1975;35:319-325.
71. Shanley DJ. Mineralizing microangiopathy: CT and MRI. *Neuroradiology*. 1995;37(4):331-333. doi:10.1007/s002340050104.
72. Suzuki S, Nishio S, Takata K, Morioka T, Fukui M. Radiation-induced brain calcification: Paradoxical high signal intensity in T1-weighted MR images. *Acta*

Neurochir (Wien). 2000;142(7):801-804. doi:10.1007/s007010070095.

73. Shepherd TM, Thelwall PE, Stanisz GJ, Blackband SJ. Chemical Fixation Alters the Water Microenvironment in Rat Cortical Brain Slices - Implications for MRI Contrast. *Proc Int Soc Magn Reson Med*. 2005;13:619.
74. Shepherd G. The Synaptic Organization of the Brain. *Oxford Univ Press*. Ch. 7. doi:10.1093/acprof:oso/9780195159561.003.0007.
75. Variola A. The ThomX Project. *2nd Int Part Accel Conf*. 2011;WEOAA01:1903-1905.
76. Larsson DH, Lundström U, Westermark UK, Henriksson MA, Burvall A, Hertz HM. First application of liquid-metal-jet sources for small-animal imaging: high-resolution CT and phase-contrast tumor demarcation. *Med Phys*. 2013;40(2):21909. doi:10.1118/1.4788661.
77. Eggl E, Schleede S, Bech M, et al. X-ray phase-contrast tomography with a compact laser-driven synchrotron source. *Proc Natl Acad Sci U S A*. 2015;112(18):5567-5572. doi:10.1073/pnas.1500938112.
78. Bidola P, Morgan K, Willner M, et al. Application of sensitive , high-resolution imaging at a commercial lab-based X-ray micro-CT system using propagation-based phase retrieval. *J Microsc*. 2017;266(2):211-220. doi:10.1111/jmi.12530.
79. Bouchet A, Bräuer-Krisch E, Prezado Y, et al. Better Efficacy of Synchrotron Spatially Microfractionated Radiation Therapy Than Uniform Radiation Therapy on Glioma. *Int J Radiat Oncol Biol Phys*. 2016;95(5):1485-1494. doi:10.1016/j.ijrobp.2016.03.040.
80. Dufort S, Le Duc G, Salomé M, et al. The High Radiosensitizing Efficiency of a Trace of Gadolinium-Based Nanoparticles in Tumors. *Sci Rep*. 2016;6:29678. doi:10.1038/srep29678.
81. Bouchet A, Lemasson B, Christen T, et al. Synchrotron microbeam radiation therapy induces hypoxia in intracerebral gliosarcoma but not in the normal brain. *Radiother Oncol*. 2013;108(1):143-148. doi:10.1016/j.radonc.2013.05.013.
82. Bartzsch S, Blattmann H, Bräuer-Krisch E, et al. Response of the rat spinal cord to X - ray microbeams. *Radiother Oncol*. 2013;106(1):106-111. doi:10.1016/j.radonc.2012.12.007.

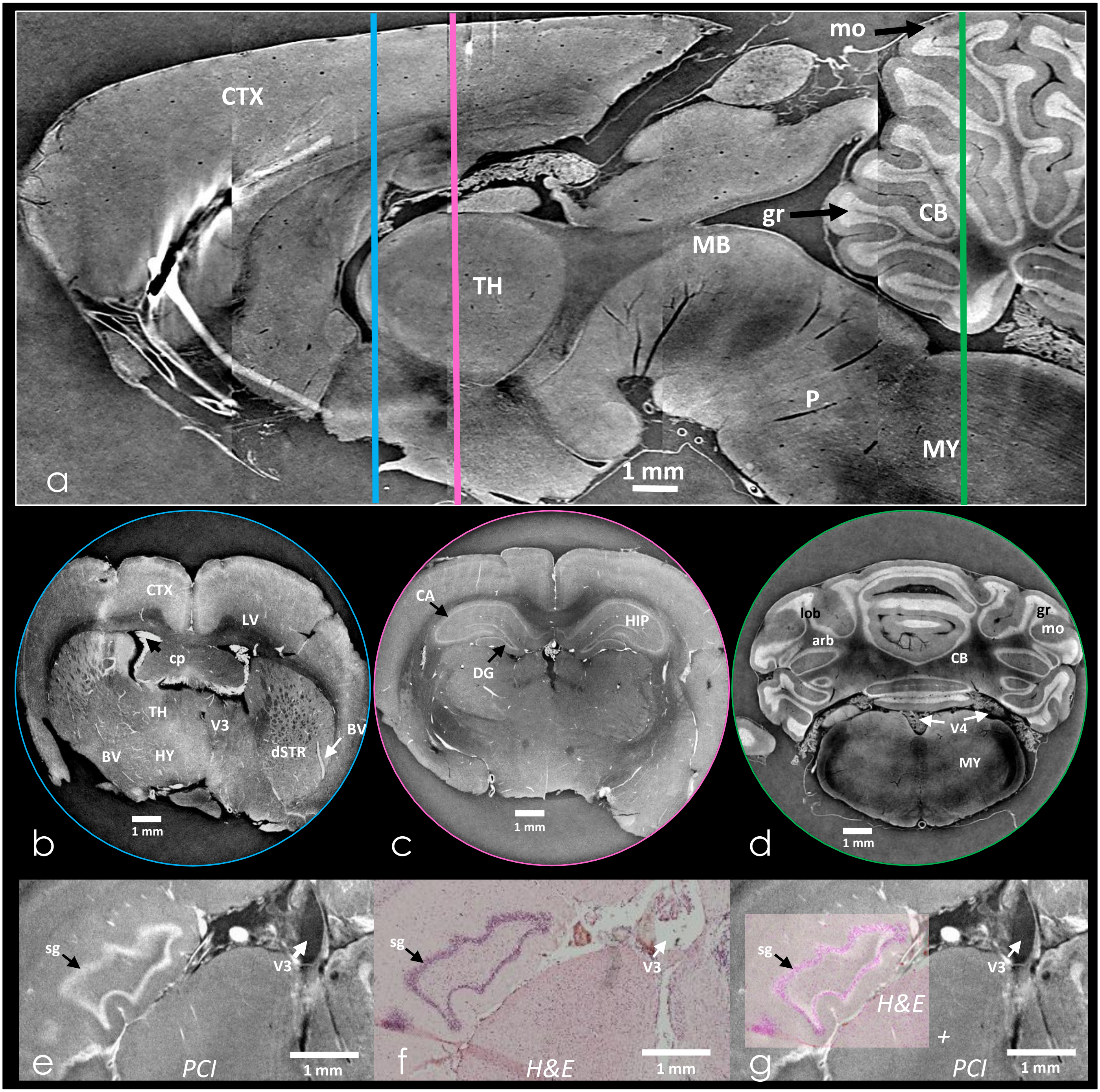
mo
CTX
gr
CB
MB
TH
P
MY
1 mm
a
CTX
LV
cp
TH
V3
BV
HY
dSTR
BV
1 mm
b
CA
HIP
DG
1 mm
c
lob
gr
mo
arb
CB
V4
MY
1 mm
d
sg
V3
e
PCI
1 mm
sg
V3
f
H&E
1 mm
sg
V3
H&E
+
g
PCI
1 mm

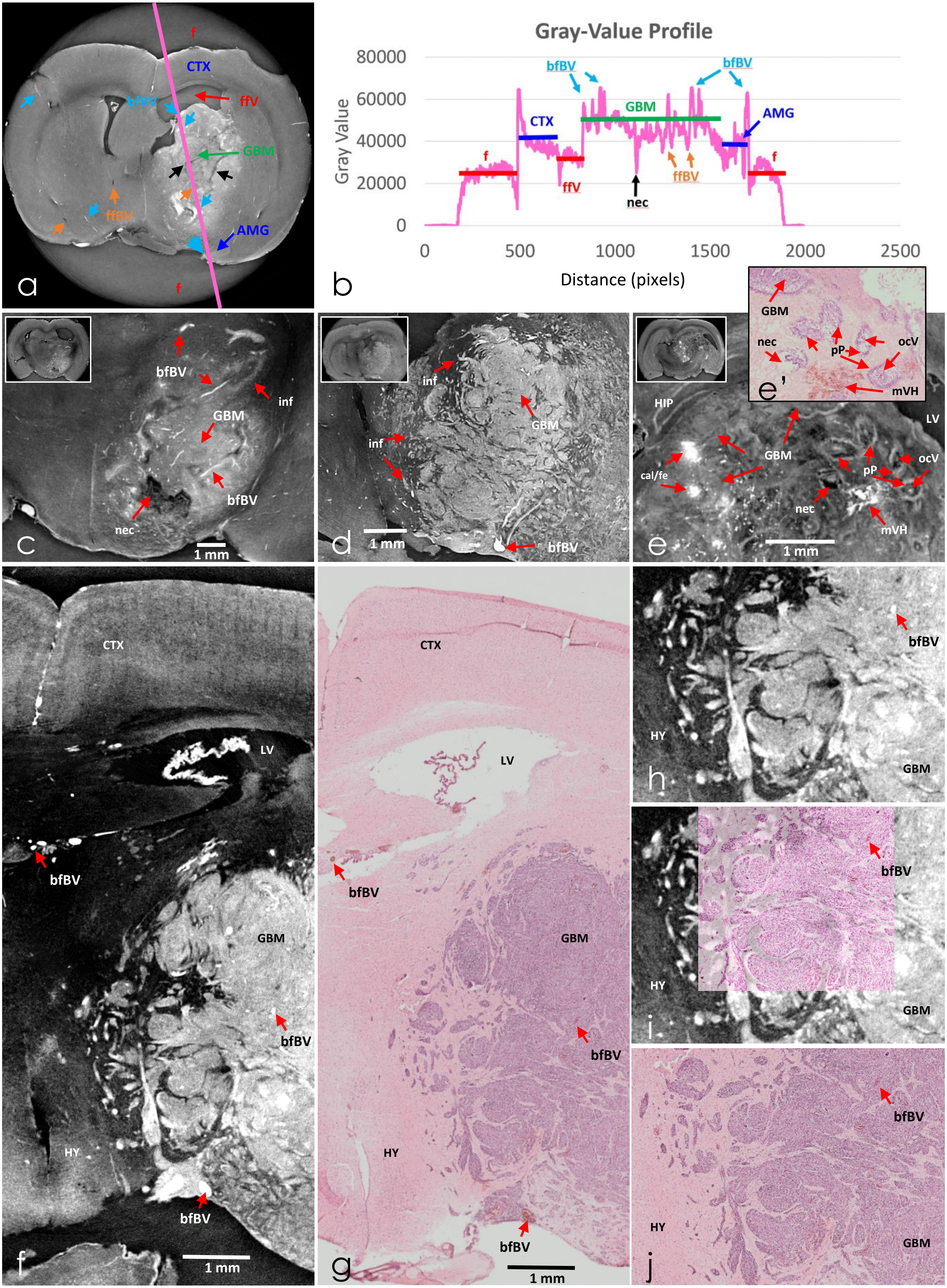
a
f
CTX
bfBV
ffV
GBM
ffBV
AMG
f
b
Gray-Value Profile
Gray Value
80000
60000
40000
20000
0
0
500
1000
1500
2000
2500
Distance (pixels)
bfBV
bfBV
CTX
GBM
AMG
f
ffV
nec
ffBV
f
e'
GBM
nec
pP
ocV
mVH
c
bfBV
inf
GBM
bfBV
nec
1 mm
d
inf
GBM
inf
bfBV
1 mm
e
HIP
LV
GBM
cal/fe
pP
ocV
nec
mVH
1 mm
f
CTX
LV
bfBV
GBM
bfBV
HY
bfBV
1 mm
g
CTX
LV
bfBV
GBM
bfBV
HY
bfBV
1 mm
h
bfBV
HY
GBM
i
bfBV
HY
GBM
j
bfBV
HY
GBM

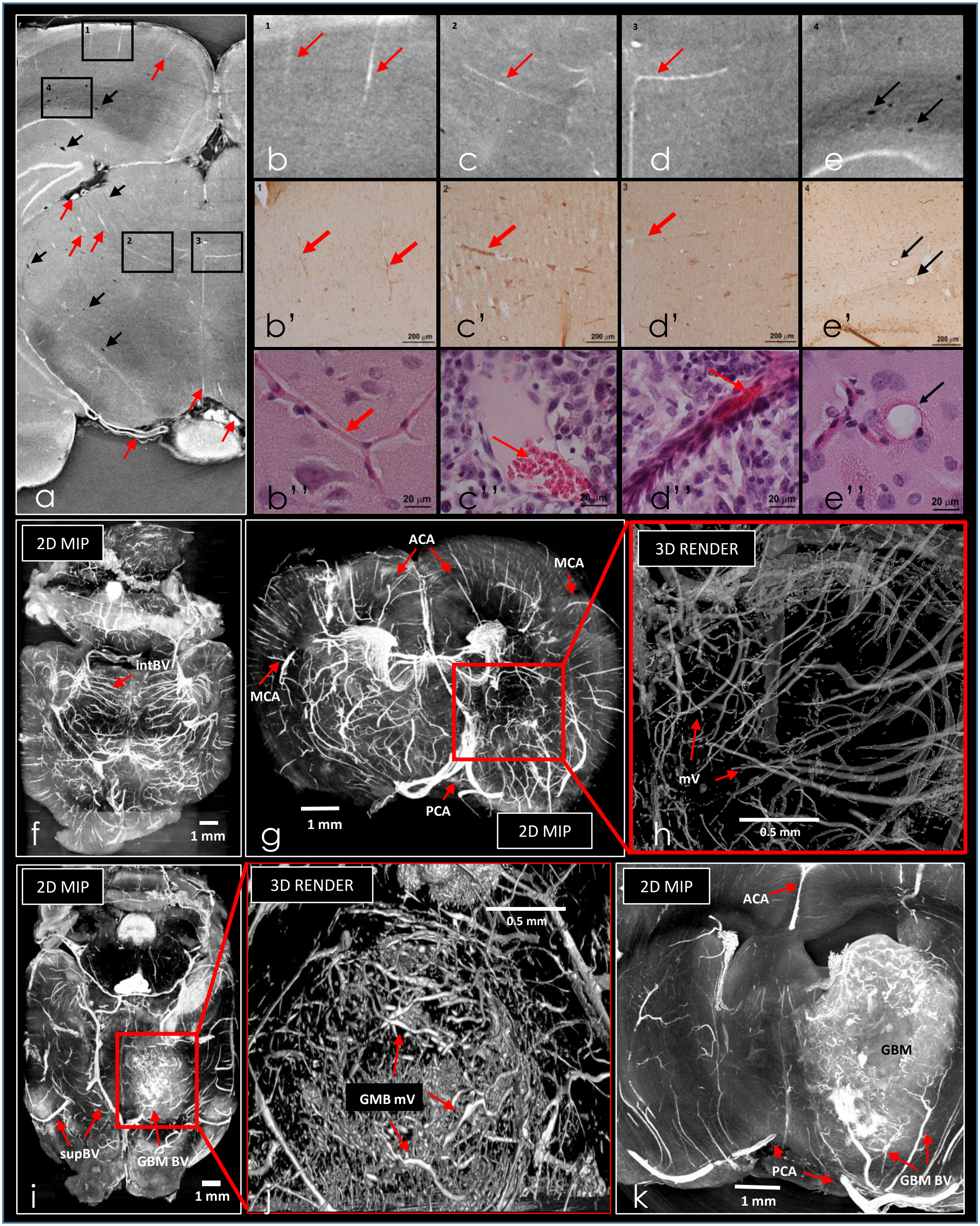
1
4
2
3
a
1
b
2
c
3
d
4
e
1
b’
200 µm
2
c’
200 µm
3
d’
200 µm
4
e’
200 µm
b’’
20 µm
c’’
20 µm
d’’
20 µm
e’’
20 µm
2D MIP
intBV
f
1 mm
ACA
MCA
MCA
PCA
1 mm
g
2D MIP
3D RENDER
mV
0.5 mm
h
2D MIP
supBV
GBM BV
i
1 mm
3D RENDER
0.5 mm
GMB mV
j
2D MIP
ACA
GBM
PCA
GBM BV
1 mm
k

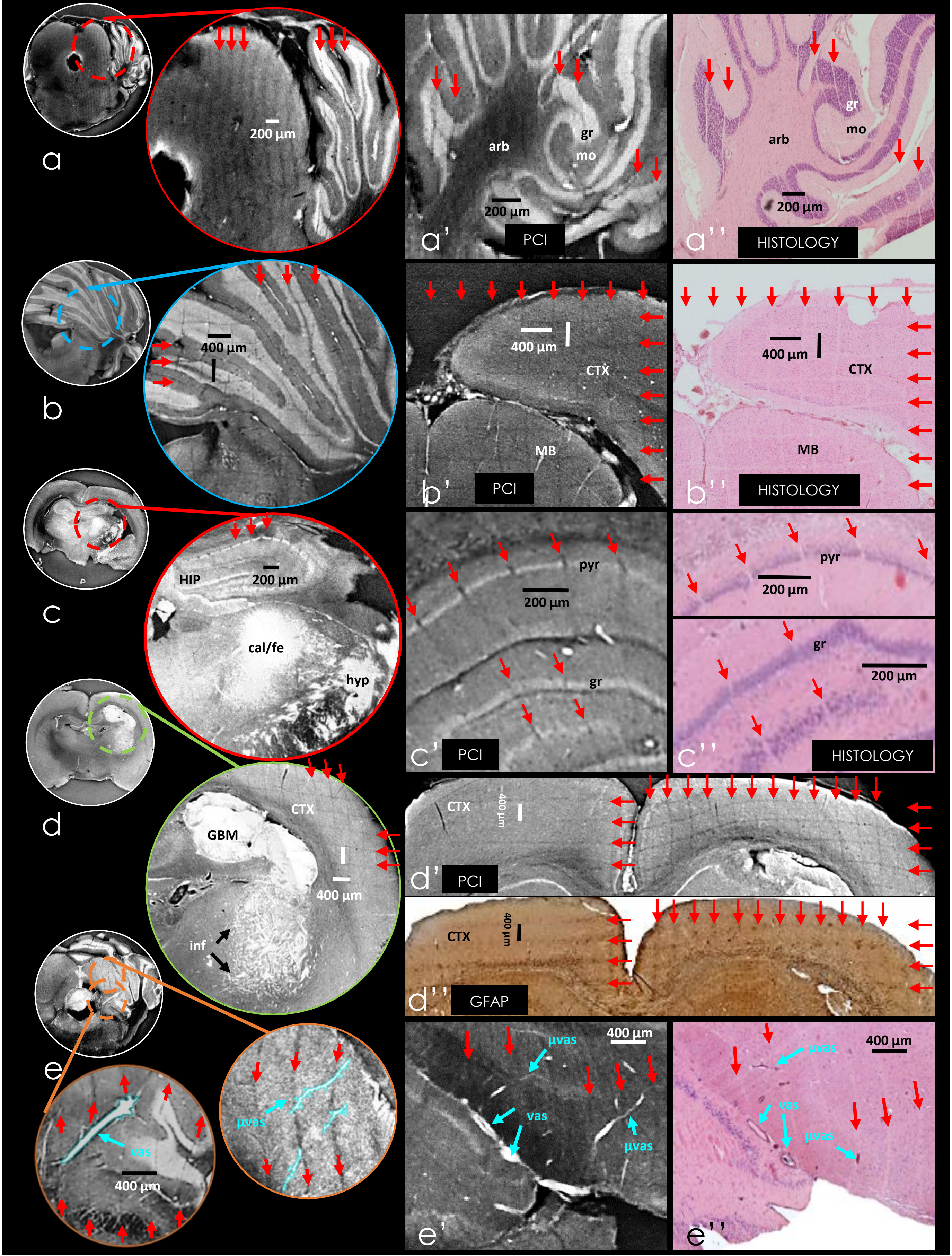
a
200 µm
arb
gr
mo
200 µm
a'
PCI
gr
mo
arb
200 µm
a''
HISTOLOGY
b
400 µm
400 µm
CTX
MB
b'
PCI
400 µm
CTX
MB
b''
HISTOLOGY
c
HIP
200 µm
cal/fe
hyp
pyr
200 µm
gr
c'
PCI
pyr
200 µm
gr
200 µm
c''
HISTOLOGY
d
CTX
GBM
400 µm
inf
CTX
400 µm
d'
PCI
CTX
400 µm
d''
GFAP
e
vas
400 µm
µvas
400 µm
µvas
vas
µvas
e'
400 µm
µvas
vas
µvas
e''

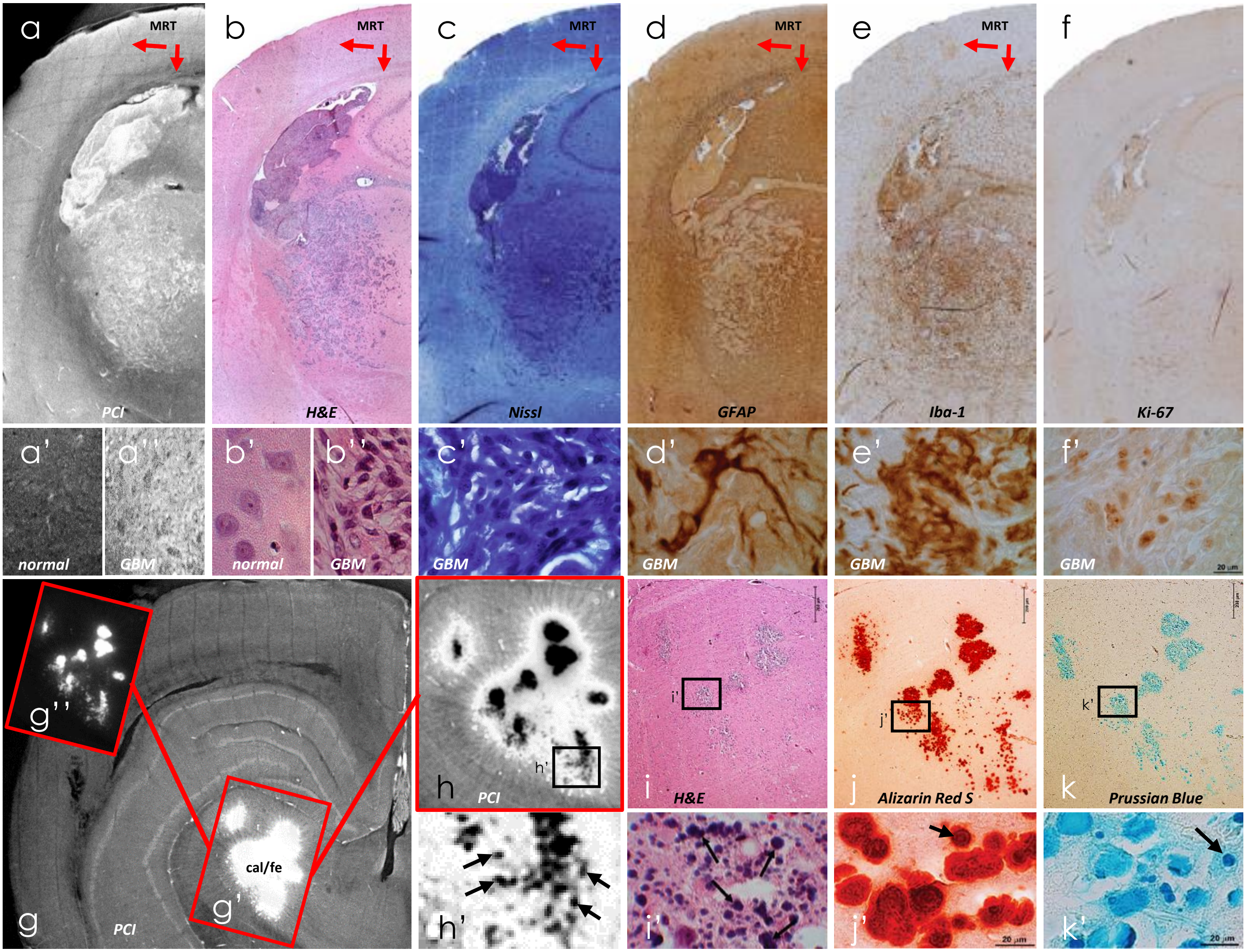
a
MRT
PCI
b
MRT
H&E
c
MRT
Nissl
d
MRT
GFAP
e
MRT
Iba-1
f
Ki-67
a'
normal
a''
GBM
b'
normal
b''
GBM
c'
GBM
d'
GBM
e'
GBM
f'
GBM
20 µm
g''
g'
cal/fe
g
PCI
h
h'
PCI
h'
i'
i
H&E
i'
j'
j
Alizarin Red S
j'
20 µm
k'
k
Prussian Blue
k'
20 µm

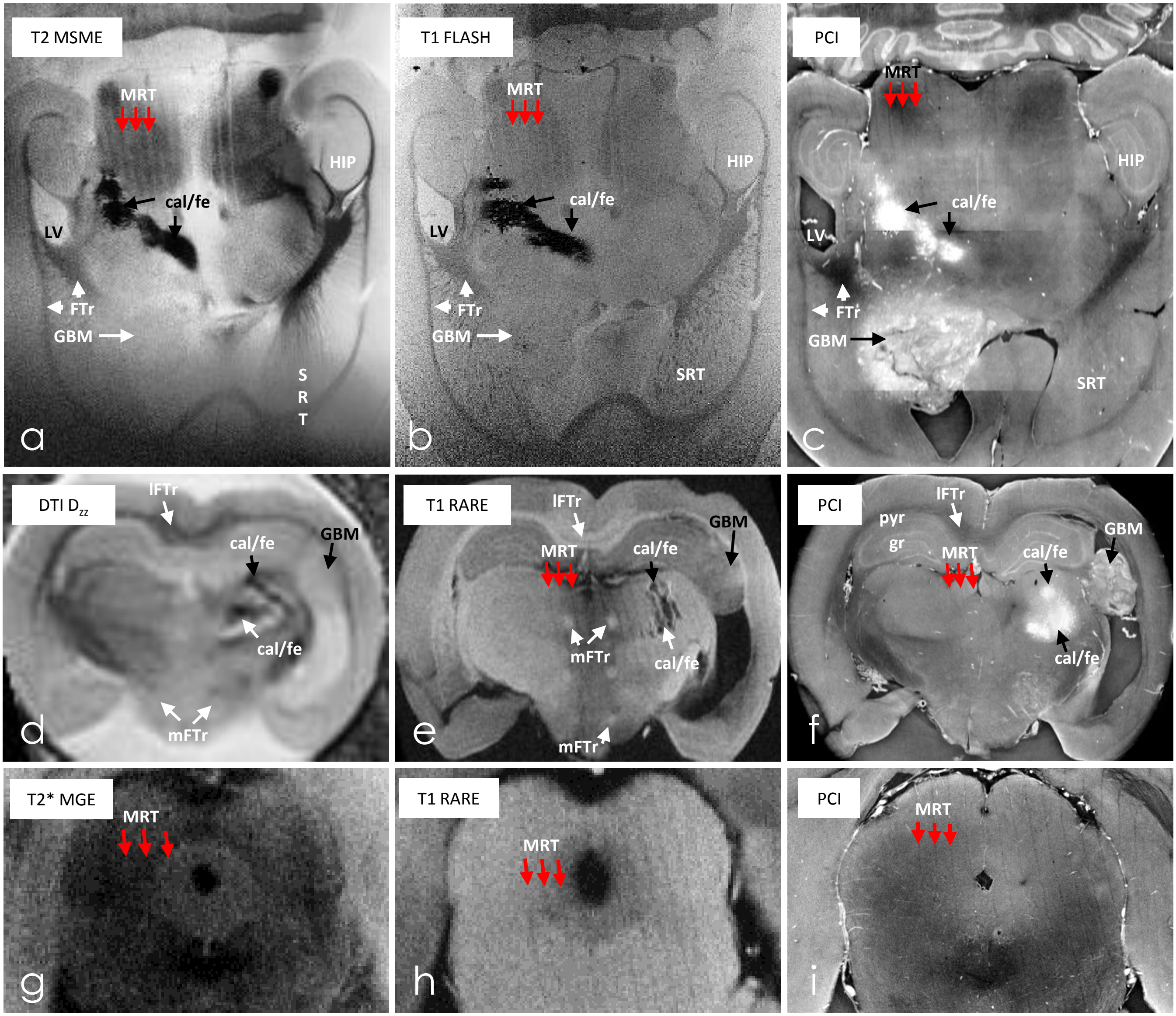
T2 MSME
MRT
cal/fe
HIP
LV
FTr
GBM
S
R
T
a
T1 FLASH
MRT
HIP
cal/fe
LV
FTr
GBM
SRT
b
PCI
MRT
HIP
cal/fe
LV
FTr
GBM
SRT
c
DTI D_{zz}
lFTr
cal/fe
GBM
cal/fe
mFTr
d
T1 RARE
lFTr
GBM
MRT
cal/fe
mFTr
cal/fe
mFTr
e
PCI
lFTr
pyr
gr
MRT
cal/fe
GBM
cal/fe
f
T2* MGE
MRT
g
T1 RARE
MRT
h
PCI
MRT
i

Summary:

Experimental X-ray Phase Contrast micro-CT provides *ex-vivo* 3D representations of *post-mortem* brain tissue and glioblastoma tumor anatomy of high sensitivity and resolution without the need for extensive sample preparation. This imaging technique proved suitable for a follow-up study of a spatially fractionated radiotherapy technique, X-ray Microbeam Radiation Therapy. We detect 50µm-thick ablations on healthy and tumor tissue, arising from locally-delivered ultra-high-dose X-ray microbeams, as well as calcium and iron accumulation within necrotic tumor tissue.